December 4, 2015
Preprint typeset using LaTeX style emulateapj v. 5/2/11

THE JCMT GOULD BELT SURVEY: A FIRST LOOK AT DENSE CORES IN ORION B

H. Kirk[1], J. Di Francesco[1, 2], D. Johnstone[1, 2, 3], A. Duarte-Cabral[4], S. Sadavoy[5], J. Hatchell[4], J.C. Mottram[5, 6], J. Buckle[7, 8], D.S. Berry[3], H. Broekhoven-Fiene[2], M.J. Currie[3], M. Fich[9], T. Jenness[3, 10], D. Nutter[11], K. Pattle[12], J.E. Pineda[13, 14, 15], C. Quinn[11], C. Salji[7, 8], S. Tisi[9], M.R. Hogerheijde[6], D. Ward-Thompson[12], P. Bastien[16], D. Bresnahan[12], H. Butner[17], M. Chen[2], A. Chrysostomou[18], S. Coude[16], C.J. Davis[19], E. Drabek-Maunder[20], J. Fiege[21], P. Friberg[3], R. Friesen[22], G.A. Fuller[14], S. Graves[3], J. Greaves[23], J. Gregson[24, 25], W. Holland[26, 27], G. Joncas[28], J.M. Kirk[12], L.B.G. Knee[1], S. Mairs[2], K. Marsh[11], B.C. Matthews[1, 2], G. Moriarty-Schieven[1], C. Mowat[4], J. Rawlings[29], J. Richer[7, 8], D. Robertson[30], E. Rosolowsky[31], D. Rumble[4], H. Thomas[3], N. Tothill[32], S. Viti[29], G.J. White[24, 25], J. Wouterloot[3], J. Yates[29], M. Zhu[33]

December 4, 2015

ABSTRACT

We present a first look at the SCUBA-2 observations of three sub-regions of the Orion B molecular cloud: LDN 1622, NGC 2023/2024, and NGC 2068/2071, from the JCMT Gould Belt Legacy Survey. We identify 29, 564, and 322 dense cores in L1622, NGC 2023/2024, and NGC 2068/2071 respectively, using the SCUBA-2 850 μm map, and present their basic properties, including their peak fluxes, total fluxes, and sizes, and an estimate of the corresponding 450 μm peak fluxes and total fluxes, using the FellWalker source extraction algorithm. Assuming a constant temperature of 20 K, the starless dense cores have a mass function similar to that found in previous dense core analyses, with a Salpeter-like slope at the high-mass end. The majority of cores appear stable to gravitational collapse when considering only thermal pressure; indeed, most of the cores which have masses above the thermal Jeans mass are already associated with at least one protostar. At higher cloud column densities, above $1 - 2 \times 10^{23}$ cm^{-2}, most of the mass is found within dense cores, while at lower cloud column densities, below 1×10^{23} cm^{-2}, this fraction drops to 10% or lower. Overall, the fraction of dense cores associated with a protostar is quite small ($< 8\%$), but becomes larger for the densest and most centrally concentrated cores. NGC 2023/2024 and NGC 2068/2071 appear to be on the path to forming a significant number of stars in the future, while L1622 has little additional mass in dense cores to form many new stars.

[1] NRC Herzberg Astronomy and Astrophysics, 5071 West Saanich Rd, Victoria, BC, V9E 2E7, Canada
[2] Department of Physics and Astronomy, University of Victoria, Victoria, BC, V8P 1A1, Canada
[3] Joint Astronomy Centre, 660 N. A'ohōkū Place, University Park, Hilo, Hawaii 96720, USA
[4] Physics and Astronomy, University of Exeter, Stocker Road, Exeter EX4 4QL, UK
[5] Max Planck Institute for Astronomy, Königstuhl 17, D-69117 Heidelberg, Germany
[6] Leiden Observatory, Leiden University, PO Box 9513, 2300 RA Leiden, The Netherlands
[7] Astrophysics Group, Cavendish Laboratory, J J Thomson Avenue, Cambridge, CB3 0HE, UK
[8] Kavli Institute for Cosmology, Institute of Astronomy, University of Cambridge, Madingley Road, Cambridge, CB3 0HA, UK
[9] Department of Physics and Astronomy, University of Waterloo, Waterloo, Ontario, N2L 3G1, Canada
[10] LSST Project Office, 933 N. Cherry Ave, Tucson, AZ 85719, USA
[11] School of Physics and Astronomy, Cardiff University, The Parade, Cardiff, CF24 3AA, UK
[12] Jeremiah Horrocks Institute, University of Central Lancashire, Preston, Lancashire, PR1 2HE, UK
[13] European Southern Observatory (ESO), Garching, Germany
[14] Jodrell Bank Centre for Astrophysics, Alan Turing Building, School of Physics and Astronomy, University of Manchester, Oxford Road, Manchester, M13 9PL, UK
[15] Current address: Max Planck Institute for Extraterrestrial Physics, Giessenbachstrasse 1, 85748 Garching, Germany
[16] Université de Montréal, Centre de Recherche en Astrophysique du Québec et département de physique, C.P. 6128, succ. centre-ville, Montréal, QC, H3C 3J7, Canada
[17] James Madison University, Harrisonburg, Virginia 22807, USA
[18] School of Physics, Astronomy & Mathematics, University of Hertfordshire, College Lane, Hatfield, HERTS AL10 9AB, UK
[19] Astrophysics Research Institute, Liverpool John Moores University, Egerton Warf, Birkenhead, CH41 1LD, UK
[20] Imperial College London, Blackett Laboratory, Prince Consort Rd, London SW7 2BB, UK
[21] Dept of Physics & Astronomy, University of Manitoba, Winnipeg, Manitoba, R3T 2N2 Canada
[22] Dunlap Institute for Astronomy & Astrophysics, University of Toronto, 50 St. George St., Toronto ON M5S 3H4 Canada
[23] Physics & Astronomy, University of St Andrews, North Haugh, St Andrews, Fife KY16 9SS, UK
[24] Dept. of Physical Sciences, The Open University, Milton Keynes MK7 6AA, UK
[25] The Rutherford Appleton Laboratory, Chilton, Didcot, OX11 0NL, UK.
[26] UK Astronomy Technology Centre, Royal Observatory, Blackford Hill, Edinburgh EH9 3HJ, UK
[27] Institute for Astronomy, Royal Observatory, University of Edinburgh, Blackford Hill, Edinburgh EH9 3HJ, UK
[28] Centre de recherche en astrophysique du Québec et Département de physique, de génie physique et d'optique, Université Laval, 1045 avenue de la médecine, Québec, G1V 0A6, Canada
[29] Department of Physics and Astronomy, UCL, Gower St, London, WC1E 6BT, UK
[30] Department of Physics and Astronomy, McMaster University, Hamilton, ON, L8S 4M1, Canada
[31] Department of Physics, University of Alberta, Edmonton, AB T6G 2E1, Canada
[32] University of Western Sydney, Locked Bag 1797, Penrith NSW 2751, Australia
[33] National Astronomical Observatory of China, 20A Datun Road, Chaoyang District, Beijing 100012, China

1. INTRODUCTION

The James Clerk Maxwell Telescope Gould Belt Survey has mapped nearly all of the nearby (∼500 pc) significant star-forming regions visible from Hawaii with the SCUBA-2 instrument (Holland et al. 2013), tracing thermal emission from dust grains at 850 μm and 450 μm (Ward-Thompson et al. 2007). A subset of these star-forming regions has also been mapped in 3–2 line emission of CO isotopologues using HARP (Buckle et al. 2009). With a variety of nearby star-forming regions mapped in a uniform manner, one of the goals of the GBS is to characterize the properties of dense cores and their surroundings, and determine the influence of the larger environment on their formation and evolution. In this paper, we present a first look at the SCUBA-2 observations of the Orion B molecular cloud using SCUBA-2, identifying dense cores and analyzing their basic properties. Buckle et al. (2010) earlier presented a first-look analysis of the ^{12}CO, ^{13}CO, and C^{18}O line observations in Orion B.

The Orion B molecular cloud is part of the larger Orion complex, a large (∼100 pc long; Maddalena et al. 1986), nearby (∼415 pc, e.g., Anthony-Twarog 1982; Menten et al. 2007) set of associated molecular clouds forming both low- and high- mass stars (e.g., Bally 2008). The best-studied part of the Orion complex is the Orion A cloud, which includes the Integral Shaped Filament (e.g., Bally et al. 1987) and the Orion Nebula Cluster (e.g., Muench et al. 2008). The Orion B cloud lies northeast of the Orion A cloud and has a similar total mass of about 10^5 M$_\odot$ (e.g., Maddalena et al. 1986; Meyer et al. 2008) but a smaller fraction of dense gas. This lower fraction of dense gas also translates into a lower overall star formation rate (two to seven times lower; Meyer et al. 2008). Lombardi et al. (2014) found that the surface density of young protostars varies roughly with the square of the extinction (or total column density) in Orion. The bulk of star formation in Orion B is concentrated within three clusters, NGC 2024, NGC 2068, and NGC 2071, which are estimated to contain 60% to 90% of the current YSOs in Orion B, while a fourth cluster, NGC 2023, is forming a smaller number of stars (e.g., Lada et al. 1991; Meyer et al. 2008). The most active parts of these four regions have been analyzed using prior submillimetre observations, including dust continuum maps from SCUBA (e.g., Motte et al. 2001; Mitchell et al. 2001; Johnstone et al. 2001, 2006; Nutter & Ward-Thompson 2007) and the polarimeter attached to SCUBA (Matthews et al. 2002; Matthews & Wilson 2002). Our SCUBA-2 observations cover a larger area around these four regions than the original SCUBA data – 2.1 and 1.7 square degrees were mapped by SCUBA-2 in NGC 2023/2024 and NGC 2068/2071 respectively, compared to 0.5 and 0.3 square degrees with SCUBA. Our SCUBA-2 observations also cover a fifth region, LDN 1622 (0.6 square degrees mapped), which contains roughly 30 YSOs (Reipurth et al. 2008). L1622 is formally part of 'Orion East' and has a different typical CO centroid velocity than the neighbouring Orion B (e.g., $\sim$ 1 km s^{-1} versus ∼10 km s^{-1}; Maddalena et al. 1986). Reipurth et al. (2008), however, cite other evidence that suggests L1622 is still part of the same Orion complex at a similar distance as Orion A and B, though a few observations suggest a distance of less than 200 pc (see discussion in Reipurth et al. 2008).

Star-forming regions tend to display hierarchical structure, as recent *Herschel* Gould Belt Survey results (e.g., André et al. 2010, 2014) have beautifully illustrated. The larger-scale (column) density distribution of material is often traced with CO observations (e.g., Maddalena et al. 1986), estimates of the dust column density based on stellar reddening (e.g., Lombardi et al. 2011), or more recently, combining *Herschel* and *Planck* measurements of dust emission (e.g., Lombardi et al. 2014). SCUBA-2 is insensitive to the largest scale of (lower) column density, like any ground-based submillimetre instrument, but provides a higher-resolution view of smaller-scale dense objects than the former measurements can usually provide. For example, Ward-Thompson et al (2015, in prep) show that in the Taurus molecular cloud, SCUBA-2 is particularly sensitive to the denser, more compact objects that will likely become (or already are) the birthsites of protostars, even when the effects of ground-based filtering are accounted for.

In our first-look analysis, we examine the dense cores detected by SCUBA-2 in the context of the larger-scale column density (using data from Lombardi et al. 2014), as well as already-formed young protostars (using data from Megeath et al. 2012 and Stutz et al. 2013). In this paper, we describe the SCUBA-2 observations (Section 2), identify the dense cores therein (Section 3), analyze the basic properties of the cores including their masses, gravitational stability, and relationship with the material in the larger cloud (Section 4), discuss our results (Section 5), and summarize our conclusions (Section 6).

2. OBSERVATIONS

Orion B was observed with SCUBA-2 (Holland et al. 2013) at 850 μm and 450 μm as part of the JCMT Gould Belt Survey (Ward-Thompson et al. 2007). Three separate regions were observed: the areas around L1622, NGC 2023/2024, and NGC 2068/2071, as illustrated in Figure 1. Our SCUBA-2 observations cover most of the high flux areas in the *Herschel* 500 μm map from Schneider et al. (2013)[34]. The SCUBA-2 observations were obtained between February 2012 and November 2014 with some initial science verification data taken in October 2011 and November 2011. Most data were observed as fully sampled 30′ diameter circular regions using the PONG 1800 mode (Kackley et al. 2010). Several science verification observations taken in the NGC 2023/2024 and NGC 2068/2071 regions were instead taken in PONG 900 mode, which fully samples a 15′ diameter circular region (Kackley et al. 2010). Each area of sky was observed between four to six times in PONG 1800 mode, with the number of repeats depending on weather conditions. Neighbouring fields were set up to overlap slightly to create a more uniform noise in the final mosaic. The PONG 900 observations are not included in the final mosaic that we analyze here, to main-

[34] We downloaded the *Herschel* 500 μm map from `http://www.herschel.fr/cea/gouldbelt/en/Phocea/Vie_des_labos/Ast/ast_visu.php?id_ast=66`

tain an approximately uniform noise level and sensitivity to larger-scale structures across the areas observed.

The data reduction used for the maps presented here follow the GBS Legacy Release 1 methodology, which is discussed in Mairs et al. (2015). The data presented here were reduced using an iterative map-making technique (makemap in SMURF[35]; Chapin et al. 2013b), and gridded to 3″ pixels at 850 μm and 2″ pixels at 450 μm. The iterations were halted when the map pixels, on average, changed by <0.1% of the estimated map rms. The initial reductions of each individual scan were coadded to form a mosaic from which a signal-to-noise mask was produced for each region. The final mosaic was produced from a second reduction using this mask to define areas of emission. In Orion B, the mask included all pixels with signal-to-noise ratio of 2 or higher at 850 μm. Testing by our data reduction team showed similar final maps using either an 850 μm-based or a 450 μm-based mask for the 450 μm reduction, when using the SNR-based masking scheme described here. Using identical masks at both wavelengths for the reduction ensures that the same large-scale filtering is applied to the observations at both wavelengths (e.g., maps of the ratio of fluxes at both wavelengths are less susceptible to differing large-scale flux recovery). Detection of emission structure and calibration accuracy are robust within the masked regions, but are less certain outside of the masked region (Mairs et al. 2015).

Larger-scale structures are the most poorly recovered outside of the masked areas, while point sources are better recovered. A spatial filter of 600″ is used during both the automask and external mask reductions, and an additional filter of 200″ is applied during the final iteration of both reductions to the areas outside of the mask. Further testing by our data reduction team found that for 600″ filtering, flux recovery is robust for sources with a Gaussian FWHM less than 2.5′, provided the mask is sufficiently large. Sources between 2.5′ and 7.5′ in diameter were detected, but both the flux and the size were underestimated because Fourier components representing scales greater than 5′ were removed by the filtering process. Detection of sources larger than 7.5′ is dependent on the mask used for reduction. At a distance of 415 pc, 7.5′ corresponds to 0.9 pc.

The data are calibrated in mJy per square arcsec using aperture flux conversion factors (FCFs) of 2.34 Jy/pW/arcsec^2 and 4.71 Jy/pW/arcsec^2 at 850 μm and 450 μm, respectively, as derived from average values of JCMT calibrators (Dempsey et al. 2013). The PONG scan pattern leads to lower noise in the map centre and mosaic overlap regions, while data reduction and emission artifacts can lead to small variations in the noise over the whole map. The pointing accuracy of the JCMT is smaller than the pixel sizes we adopt, with current rms pointing errors of 1.2″ in azimuth and 1.6″ in elevation (see `http://www.eaobservatory.org/JCMT/telescope/pointing/pointing.html`); JCMT pointing accuracy in the era of SCUBA is discussed in Di Francesco et al. (2008).

The observations for Orion B were taken in both grade one ($\tau_{225GHz} < 0.05$) and grade two ($0.05 < \tau_{225GHz} < 0.08$) weather, corresponding to $\tau_{850\ \mu m} < 0.21$ and $0.21 < \tau_{850\ \mu m} < 0.34$ respectively (Dempsey et al. 2013), with a mean value of τ_{225GHz} of 0.06 ± 0.01. At 850 μm, the final noise level in the mosaic is typically 0.05 mJy arcsec^{-2} per 3″ pixel, corresponding to 3.7 mJy per 14.6″ beam. At 450 μm, the final noise level is 1.2 mJy arcsec^{-2} per 2″ pixel, corresponding to 59 mJy per 9.8″ beam. (Note the beamsizes quoted here are the effective beams determined by Dempsey et al. 2013, and account for fact that the beam shape is well-represented by the sum of a Gaussian primary beam shape and a fainter, larger Gaussian secondary beam). The noise levels for each PONG observing area in the final mosaic is given in Table 1 in terms of the typical rms in a pixel.

Figures 2 through 4 show the final reduced images, along with their associated noise maps. The external masks applied are indicated by the blue contours on the 850 μm noise map. Note that the isolated pixels in the mask at the map edges will have no effect on the scale of a dense core, since the contiguous area within those parts of the mask is too small. Several of the brightest sources of emission in the maps are surrounded by negative ('bowl') features. These features may slightly diminish the sizes and total fluxes we derive for sources in Section 3, but based on artificial source-recovery tests discussed in Mairs et al. (2015) and our mask-making strategy, we expect our results to be accurate to 20% or better.

Portions of the NGC 2023/2024 and NGC 2068/2071 regions were also observed by the GBS in ^{12}CO(3-2) with HARP (Buckle et al. 2010) and reduced using ORAC-DR (Jenness et al. 2015). These areas are indicated as contours in Figures 1, 3, and 4. The ^{12}CO (3-2) emission line lies within the 850 μm continuum band, and therefore some fraction of the 850 μm flux may in fact not be thermal dust emission (e.g., Johnstone et al. 2003). Observations of other star-forming regions (e.g., Johnstone et al. 2003; Drabek et al. 2012; Sadavoy et al. 2013; Hatchell et al. 2013; Pattle et al. 2015; Salji et al. 2015; Buckle et al. 2015) have shown that this 'contamination' is generally not a large effect (< 20%), the main exception being regions with faint dust emission and bright CO outflows, where the ^{12}CO emission can dominate (up to 90%). Over the regions where we have HARP CO observations, we estimate the level of CO contamination on the observed 850 μm flux. Following the procedure outlined in Drabek et al. (2012), we run an extra round of data reduction with the CO integrated intensity map included as a negative source of emission in each raw datafile, scaled to the atmospheric transmission of that evening. These CO-subtracted maps are then mosaicked together, and compared with the original 850 μm mosaic. This procedure ensures that the CO data are filtered and processed identically to our 850 μm data. We calculate the fractional CO contamination level as

$$f_{CO} = \frac{S_{850,orig} - S_{850,noco}}{S_{850,orig}} \quad (1)$$

where $S_{850,orig}$ is the flux in the original 850 μm map and $S_{850,noco}$ is the flux in the CO-subtracted 850 μm map. Most of the area mapped has f_{CO} below the (fractional) noise level at the same location, implying an overall very small contamination level. In NGC 2068/2071, several

[35] SMURF is a software package used for reducing JCMT observations, and is described in more detail in Chapin et al. (2013a).

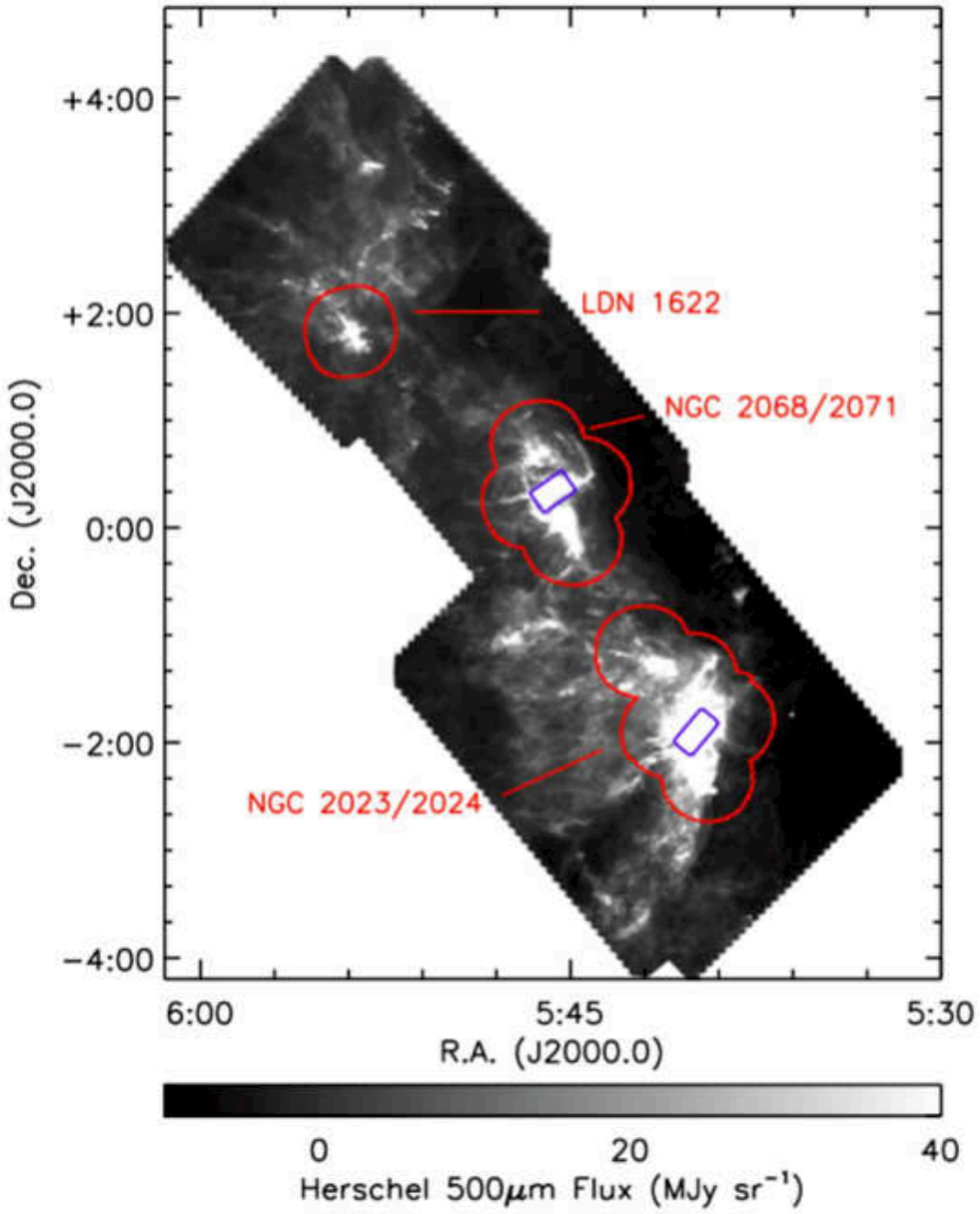

Figure 1. The areas observed by SCUBA-2 in Orion B. The background image shows the 500 μm flux measured by *Herschel*, while the red contours show the areas observed with SCUBA-2, and the blue contours show the areas observed in CO(3–2) with HARP.

small zones at the outskirts of the NGC 2071 cluster show f_{CO} above the 20% level, but these are generally in areas of lower 850 μm flux. In NGC 2023/2024, slightly off of the main NGC 2024 cluster, there are several dense cores which show contamination levels above 50% over part of their extent (less than half of their full extent, and usually substantially less). In general, however, the level of CO contamination is small. Since most of the cores fall outside of the region with CO observations, we do not include the CO flux corrections in any of our subsequent analysis.

3. SOURCE IDENTIFICATION

We identify cores in the three 850 μm Orion B maps using FellWalker (Berry 2015), a source identification algorithm available as part of the CUPID[36] package (Berry et al. 2007) in Starlink. The basic premise of FellWalker is to define the peaks and sizes of objects in images based on local gradients, and the extent of pathways which lead to a given peak. Like the more traditionally-used ClumpFind algorithm (Williams et al. 1994), FellWalker does not assume a geometry when identifying cores. ClumpFind, however, splits zones of complex emission into multiple cores based on user-selected con-

[36] `http://www.starlink.ac.uk/cupid`

Table 1
Noise per area observed

Region	Name[a]	R.A.[b] (J2000.0)	decl.[b] (J2000.0)	σ_{850}[c] (mJy arcsec^{-2})	σ_{450}[c]	σ_{850}[d] (mJy bm^{-1})	σ_{450}[d]	N_{obs}[e]
LDN 1622	ORIONBN_850_solo	5:54:33	1:49:34	0.053	2.0	3.9	98	6
NGC 2068/2071	ORIONBN_450_E	5:47:55	0:13:60	0.050	1.0	3.7	49	6
NGC 2068/2071	ORIONBN_450_S	5:46:17	0:06:30	0.050	1.2	3.7	59	6
NGC 2068/2071	ORIONBN_450_W	5:45:55	0:24:42	0.055	1.7	4.0	84	6
NGC 2068/2071	ORIONBN_850_N	5:47:33	0:45:26	0.047	0.9	3.4	44	6
NGC 2023/2024	ORIONBS_450_E	5:42:38	-1:54:19	0.049	1.1	3.6	54	6
NGC 2023/2024	ORIONBS_450_S	5:41:16	-2:18:26	0.051	0.8	3.7	39	4
NGC 2023/2024	ORIONBS_450_W	5:40:34	-1:48:26	0.052	0.9	3.8	44	4
NGC 2023/2024	ORIONBS_850_N	5:43:39	-1:09:11	0.047	1.0	3.4	49	6
NGC 2023/2024	ORIONBS_850_S	5:41:53	-1:24:41	0.043	1.2	3.1	59	7

[a] Observation designation chosen by GBS team, denoted as Target Name in the CADC database at `http://www3.cadc-ccda.hia-iha.nrc-cnrc.gc.ca/en/jcmt/`
[b] Central position of each observation
[c] Pixel-to-pixel (rms) noise for the final mosaic of all of the observed PONG 1800s for the given area at 850 μm and 450 μm respectively.
[d] Effective noise per beam (i.e., point source sensitivity) for the final mosaic of all of the observed PONG 1800s for the given area at 850 μm and 450 μm respectively.
[e] Total number of PONG 1800 observations taken at each wavelength. Note that this count may include partially completed scans.

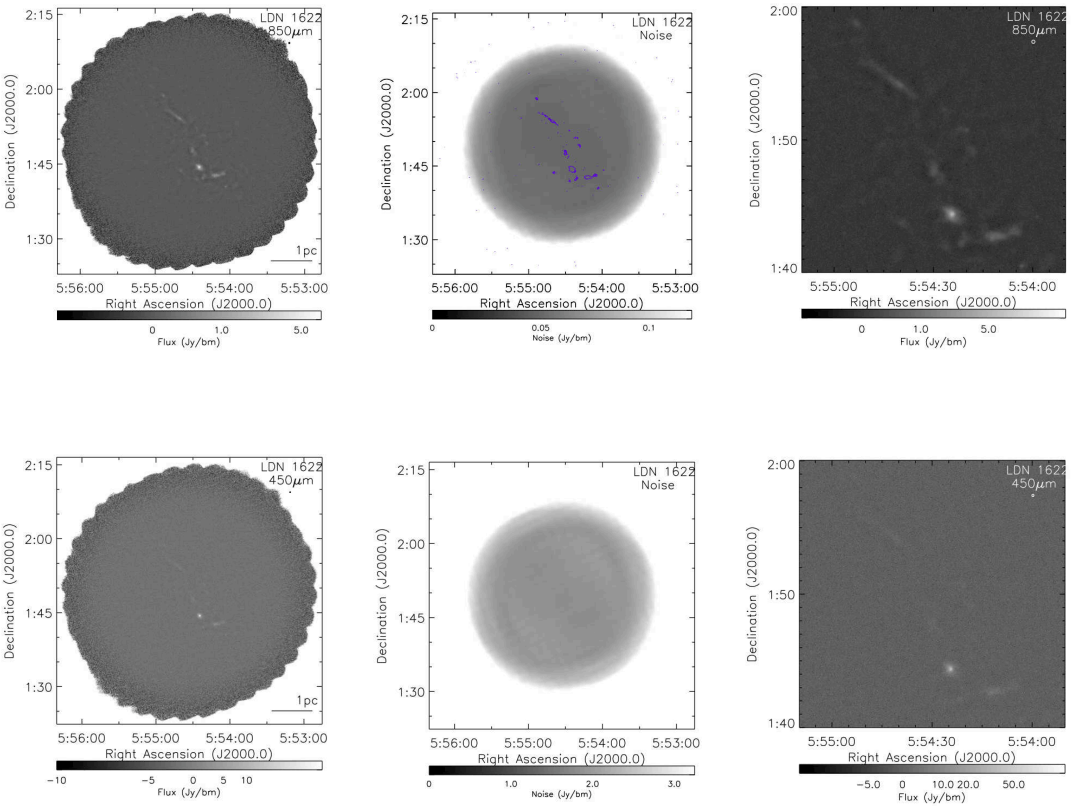

Figure 2. The SCUBA-2 850 μm (top) and 450 μm (bottom) observations of L1622 in Orion B. The left panel on each row shows the entire map, while the middle panel shows the noise, and the right panel shows a zoom on a zone of stronger emission. In the left and right panels, the scaling is approximately logarithmic, while the middle panel is shown with a linear scale. The black circle in the upper right corner shows the effective beamsize at each wavelength, while the scale bar at the bottom indicates the angular distance corresponding to 1 pc at the assumed cloud distance of 415 pc. The external mask used in the reduction is indicated by the blue contour on the 850 μm noise map (signal-to-noise ratio ≥ 2 at 850 μm in the initial reduction). An identical mask was used at 450 μm.

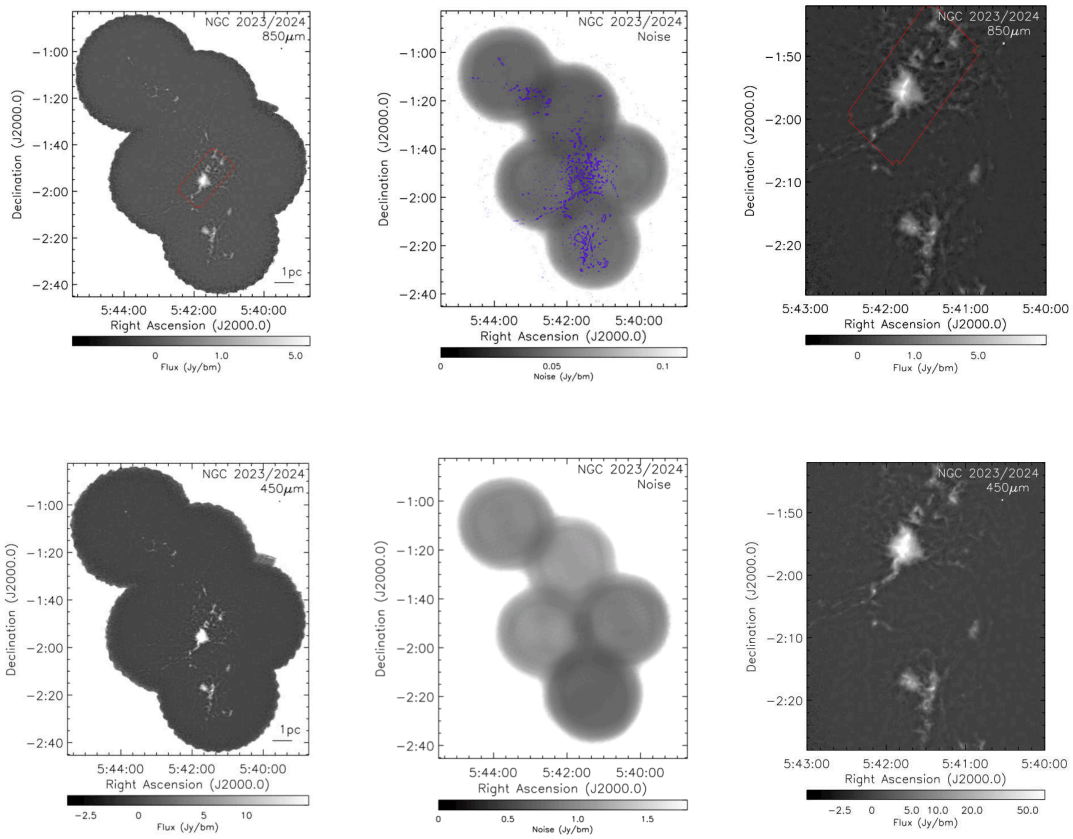

Figure 3. The SCUBA-2 850 μm (top) and 450 μm (bottom) observations of NGC 2023/2024 in Orion B. See Figure 2 for the plotting conventions used. The red contours on the left and right panels indicate regions with GBS HARP CO observations.

tour levels, whereas FellWalker relies on local gradients instead; Watson (2010) found FellWalker generally produces superior results to ClumpFind, including a generally better recovery of accurate peak and total fluxes of artifical cores inserted into maps. FellWalker provides both a listing of the peak flux position for each dense core and also a dense core footprint (i.e., a set of pixels all belonging to the core). Appendix A discusses the details of our source identification process.

We ran FellWalker with very relaxed settings, identifying 260, 1383, and 1020 potential sources, from which we then culled unreliable sources from. After this subsequent elimination, we identified 29 reliable cores in L1622, 564 in NGC 2023/2024, and 322 in NGC 2068/2071. See Appendix A for more details on our core identification strategy. Our final core list includes cores with peaks potentially as low as twice the local noise level. While this is fainter than most core searches would be extended to, a careful comparison of the 850 μm data with the *Herschel* 500 μm data revealed that faint structures below the formal 3σ typical cutoff were, in fact, real, and appear to have similar extents at both wavelengths. The dense cores we identify are shown in Figures 5 through 7, with the dense core footprints, and the *Spitzer*-identified protostars from Megeath et al. (2012) and *Herschel*-identified protostars from Stutz et al. (2013) also shown (see next section for more discussion on identifying protostellar cores). We note that in Figure 5, more closed contours are apparent than the total number of cores identified. *FellWalker* does not require that cores have contiguous boundaries, and therefore sometimes near a core edge, some pixels will be excluded, e.g., due to low flux, while other neighbouring pixels do satisfy all of the core criterion and are included. These isolated pixels represent a small fraction of individual cores and by definition are located in low-flux areas of the map. Therefore, these isolated pixels have minimal influence on the properties we measure (recall that the core size is based on the total area of the core footprint, not the maximal core extent).

Table 4 provides a full list of the dense cores we identify within each of the three regions. In the table, core locations correspond to the position of peak flux within the core. The peak flux and total flux are calculated without any background emission subtracted, but see Section 4 for further treatment of this issue. The peak flux is given in Jy bm^{-1}, with the conversion from mJy arcsec^{-2} made assuming an effective beam size of 14.6 $''$ (Dempsey et al. 2013). The core size is the effective radius, R_{eff}, calculated as the radius of a circle which spans the same area as the dense core (calculated using the full dense core footprint). For cores where HARP CO observations were made, we also include the fraction of the core's area covered by the CO data, and the resulting core peak fluxes and total fluxes at 850 μm with the contribution from CO emission removed. We also calculate the peak and total 450 μm flux using the same dense core footprints as the 850 μm data. Note that we do not make any attempt to account for the noise level at 450 μm within the dense core footprints. In effect, cores with little to no 450 μm emission above the noise level may have a negative total flux within the core footprint.

The original SCUBA instrument at JCMT observed parts of NGC 2023/2024 and NGC 2068/2071 (e.g., Motte et al. 2001; Mitchell et al. 2001; Johnstone et al. 2001, 2006; Nutter & Ward-Thompson 2007). Motte et al. (2001) used a wavelet-based scheme to identify dense cores, which generally identifies more compact regions of emission. Other SCUBA analyses (Mitchell et al. 2001; Johnstone et al. 2001, 2006; Nutter & Ward-Thompson 2007) used ClumpFind, which tends to act more similarly to FellWalker, in identifying larger zones of emission around each core. We provide a detailed comparison of the dense cores identified in Nutter & Ward-Thompson (2007) as well as those published in the SCUBA Legacy Catalogue (Di Francesco et al. 2008) with our SCUBA-2 results in Appendix B. We find generally good agreement between the cores identified in SCUBA and their corresponding match in the SCUBA-2 data. Different core identification schemes, however, can subdivide regions of complex emission differently, which generally leads to larger differences in the total fluxes and sizes of the cores between the two measurements than peak fluxes. The SCUBA-2 observations are factors of four to six times more sensitive than the SCUBA observations, with a median noise level of 3.7 mJy bm^{-1} compared to 16-23 mJy bm^{-1} in SCUBA (Nutter & Ward-Thompson 2007).

4. DENSE CORE PROPERTIES

We first classify all of the dense cores as starless or protostellar. Our aim is to make a conservative list of starless cores. We start by using the *Spitzer* catalogue from Megeath et al. (2012) to identify protostars. Specifically, any dense core which contained one or more protostars listed in the 'all protostars' list from Megeath et al. (2012) within the dense core's boundary was classified as protostellar. We supplement our list of protostars by running a similar procedure on the full list of candidate protostars from Stutz et al. (2013) using *Herschel* data. In other words, if any pixel of a core has a protostar lying within it from either catalogue, we classify the core as protostellar. We note that the *Herschel* catalogue covers a smaller area within Orion B, and focuses exclusively on the most embedded YSOs. This procedure allows us to identify five protostellar cores in L1622, 25 in NGC 2023/2024 (of which 3 were *Herschel*-based) and 34 in NGC 2068/2071 (of which 6 were *Herschel*-based). The number of starless cores in each region is therefore 24, 539, and 288 in L1622, NGC 2023/2024, and NGC 2068/2071 respectively. Table 4 denotes which dense cores we defined as protostellar.

4.1. *Masses*

In addition to the dense core properties returned directly from FellWalker (size, peak flux, and total flux), the core mass is an important property. Using only the total 850 μm flux measured for each core, we estimate the mass using the equation

$$M = \frac{S_\nu D^2}{\kappa_\nu B_\nu(T)} \tag{2}$$

from Hildebrand (1983), where S_ν is the total flux at frequency ν, κ is the dust opacity, and B is the black

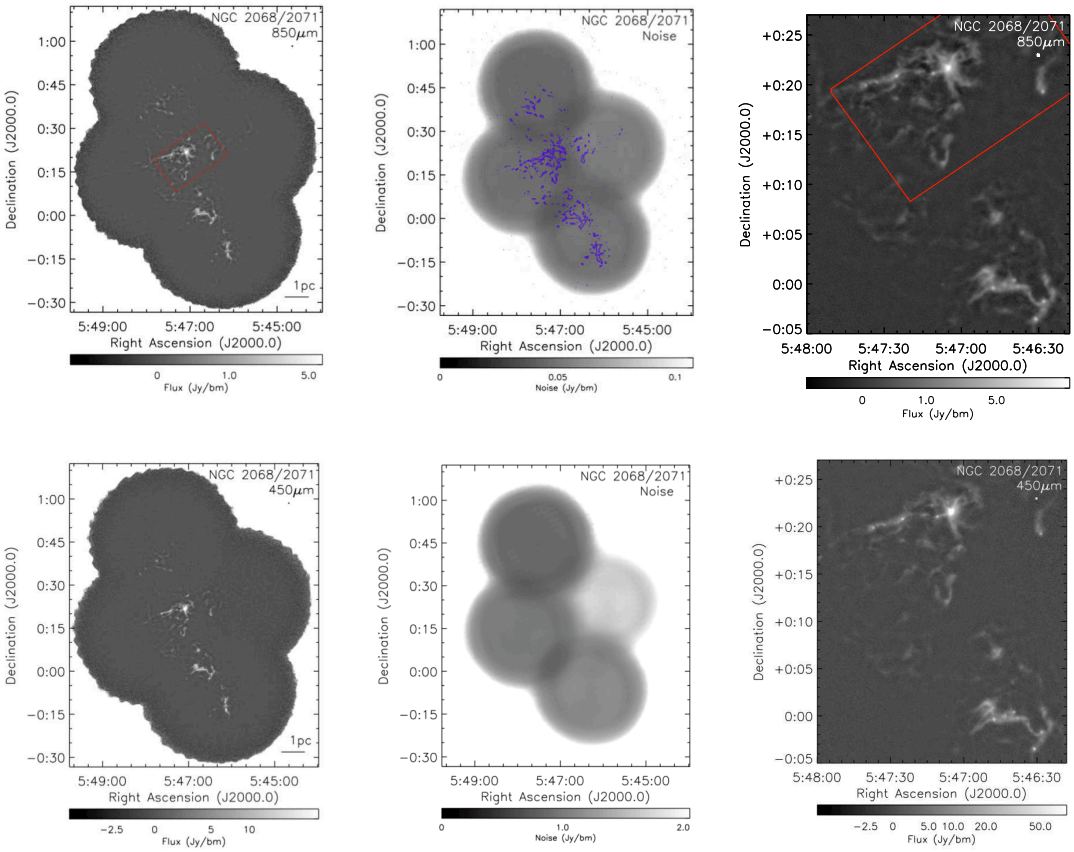

Figure 4. The SCUBA-2 850 μm (top) and 450 μm (bottom) observations of NGC 2068/2071 in Orion B. See Figure 3 for the plotting conventions used.

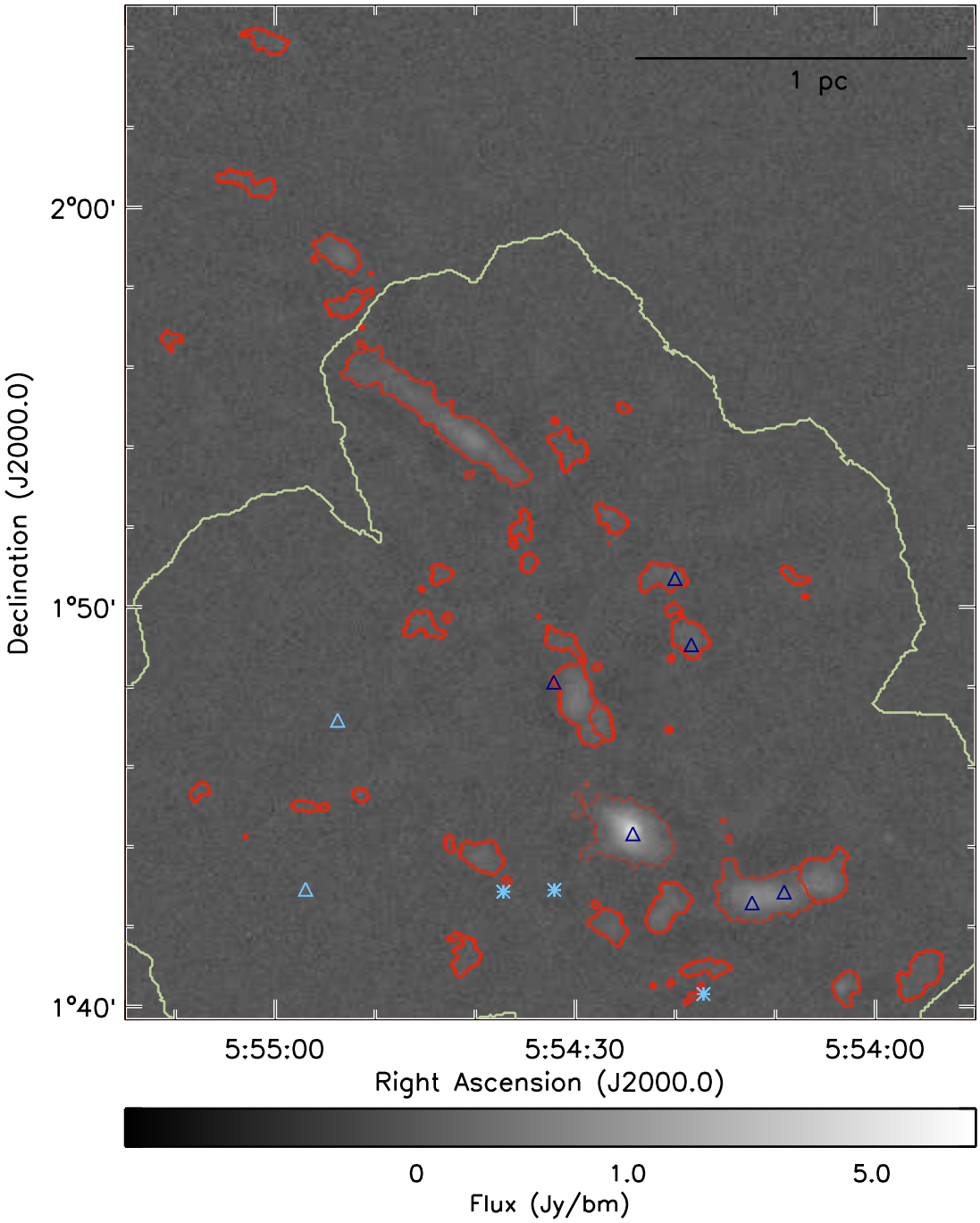

Figure 5. Dense cores identified in L1622. The background greyscale image shows the SCUBA-2 850 μm emission. The red contours show the dense core boundaries, as identified with FellWalker, while the blue triangles show locations of protostars from the *Spitzer* YSO catalogue of Megeath et al. (2012) and blue asterisks show the *Herschel* YSO catalogue of Stutz et al. (2013). Dark symbols indicate protostars associated with a dense core, while light symbols indicate unassociated protostars. The light yellow contour denotes the *Herschel* coverage for the Stutz et al. (2013) catalogue (A. Stutz, priv. comm.).

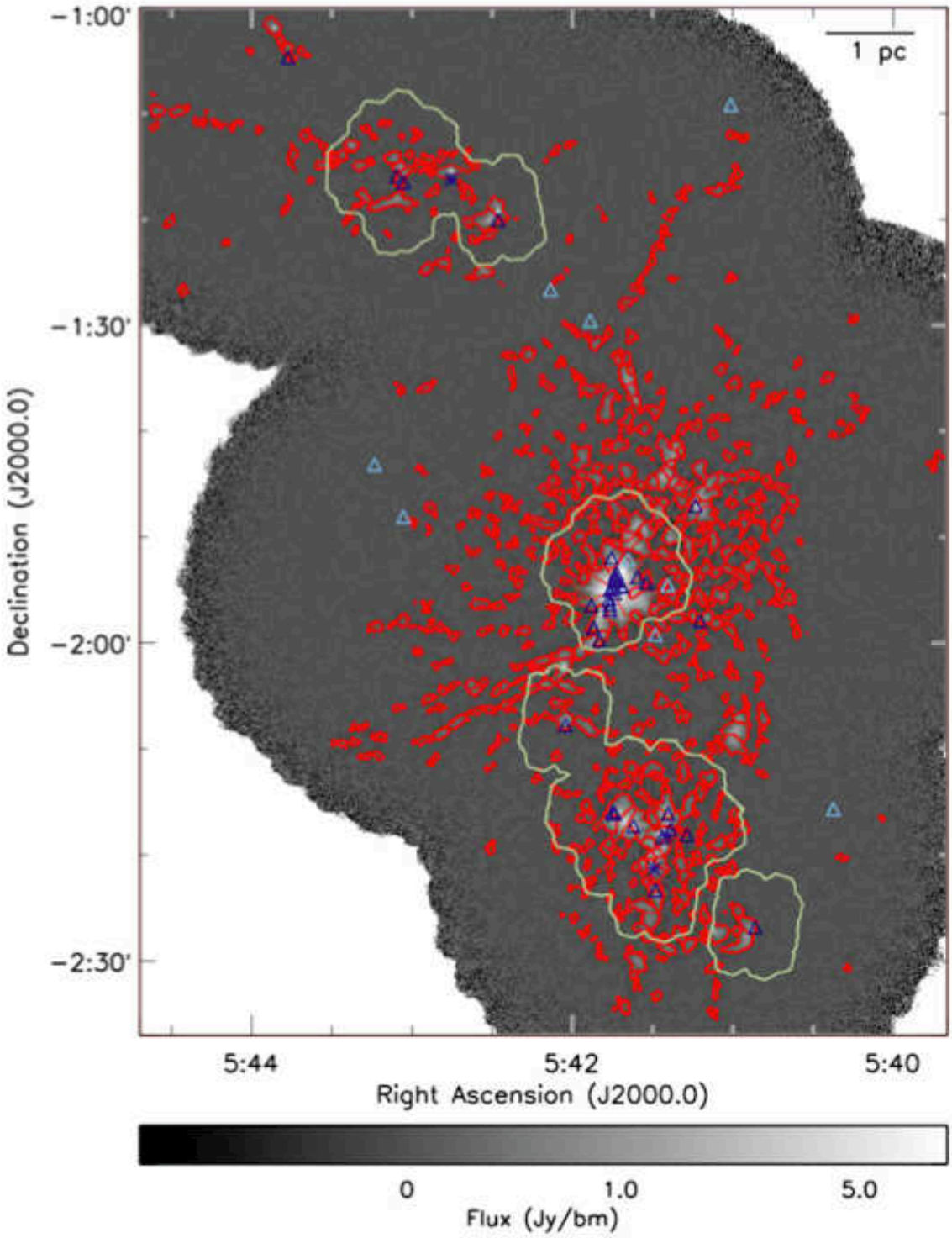

Figure 6. Dense cores identified in NGC 2023/2024. See Figure 5 for the plotting conventions used.

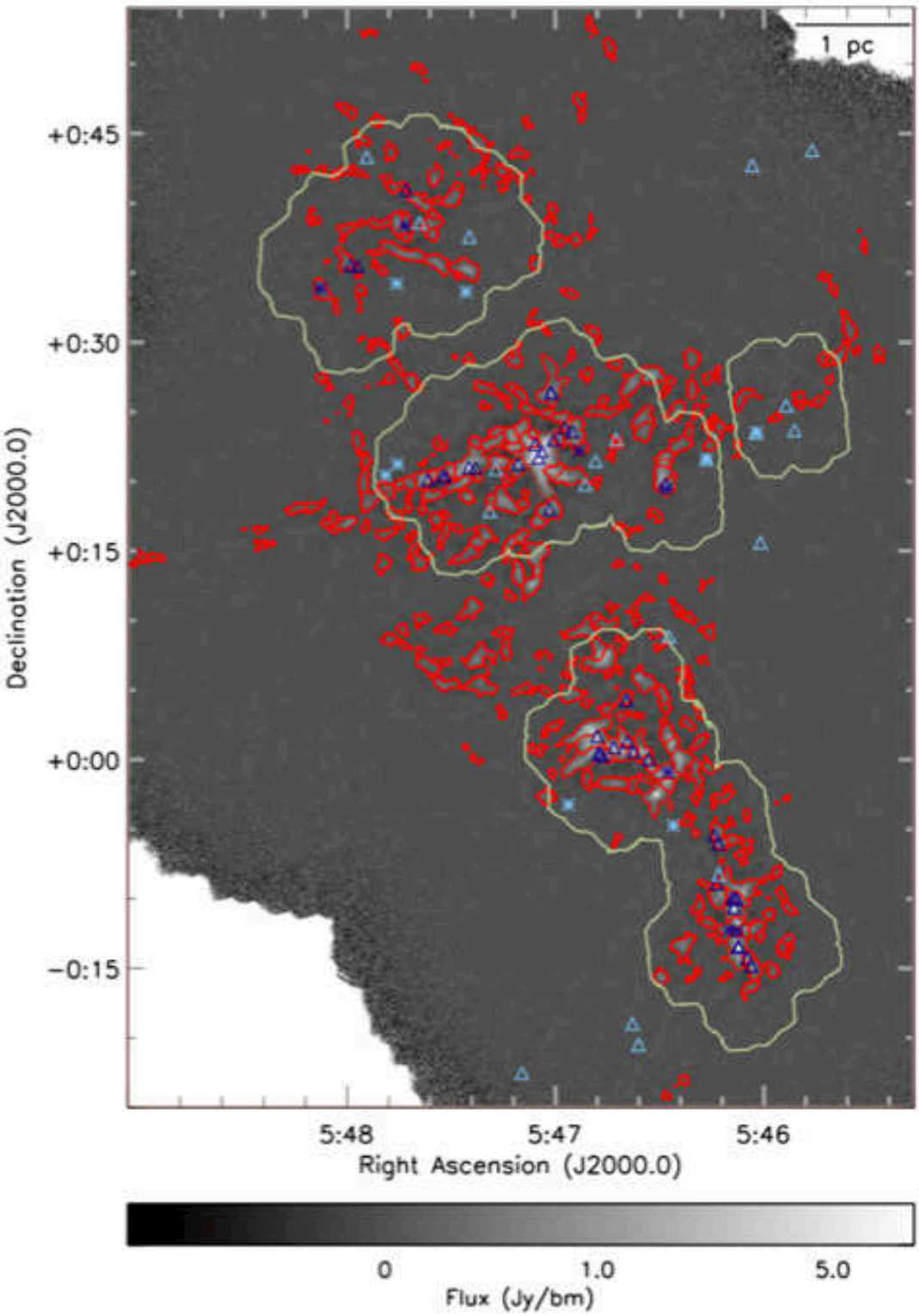

Figure 7. Dense cores identified in NGC 2068/2071. See Figure 5 for the plotting conventions used.

body function at temperature T. This simplifies to

$$M = 1.06 \times S_{850\ \mu m} \times (e^{\frac{17\ K}{T}} - 1) \times (\kappa_{850\ \mu m}/0.0125\, cm^2\ g^{-1})^{-1} \times (D/415\ pc)^2 \quad (3)$$

with M in solar masses and $S_{850\ \mu m}$ in Jy bm^{-1}. We adopt a dust opacity of $\kappa_\nu = 0.1 \times (\nu/10^{12} Hz)^\beta$ cm^2 g^{-1} with $\beta = 2$, i.e., $\kappa_{850\mu m} = 0.0125$ cm^2 g^{-1}, following Pattle et al. (2015) and Salji et al. (2015) among others, and a distance of 415 pc following Buckle et al. (2010). These two assumptions are similar to those used in previous SCUBA analyses. Note, however, that Motte et al. (2001), Johnstone et al. (2006), and Nutter & Ward-Thompson (2007) assume a distance of 400 pc, while Johnstone et al. (2001) assumes 450 pc. Also, Johnstone et al. (2001) and Nutter & Ward-Thompson (2007) assume $\kappa_{850} = 0.01$ cm^2 g^{-1} while Motte et al. (2001) and Johnstone et al. (2006) assume $\kappa_{850} = 0.02$ cm^2 g^{-1}.

The dense cores are likely to have a range of temperatures (both within each core, and core-to-core), although the largest variation would be expected for the protostellar cores. Schneider et al. (2013) find dust temperatures of $\sim$ 20 K or higher around the NGC 2023/2024 and NGC 2068/2071 clusters, where most of the SCUBA-2 emission is observed[37]. We therefore assume a constant temperature of 20 K, consistent with Johnstone et al. (2006) and Nutter & Ward-Thompson (2007), as well as Sadavoy et al. (2010); Motte et al. (2001), however, assumed a temperature of 15 K for starless cores and 20-40 K for protostellar cores, while Johnstone et al. (2001) assumed a constant value of 30 K. Johnstone et al. (2006) note the four most massive cores they identified in Orion B are known to harbour bright far infrared sources which have heated them to above 50 K, which would lower their estimated masses considerably from the value measured assuming 20 K. At 50 K, the masses would be a factor of 3.3 lower than assuming a temperature of 20 K. We expect high temperatures to be most likely in some of the brightest protostellar cores, where the masses we estimate are largest. Uncertainties in the dust opacity and cloud distance also increase the uncertainty in the dense core mass estimates. The dust opacity at 850 μm likely has some variation across the cloud, with some inter-core and core-to-core variations, as seen in the β variations measured across the Perseus molecular cloud by Chen et al (2015, submitted) and Sadavoy et al. (2013). We expect that the distance will generally be relatively constant across the cloud, and is more likely to affect global population values (i.e., changes would increase / decrease all masses by the same factor), and should have a smaller effect on the relative masses estimated.

In addition to the uncertainties in the conversion factor between flux and mass, there is one other important consideration. Structures within molecular clouds are hierarchical in nature, although our SCUBA-2 observations are insensitive to the largest of these structures. Source identification algorithms such as FellWalker associate zones of emission with a single source, whereas other types of algorithms such as those based on dendrograms (e.g., Rosolowsky et al. 2008) treat emission as nested levels in a hierarchy of emission. Under the latter scheme, only a fraction of the total emission at a given position would be associated with the top level of the hierarchical structure (i.e., the dense core), while some fraction of the emission would be associated with underlying larger structures. We therefore make a second estimate of the total flux associated with each core which accounts for some of this larger-scale structure. Conservatively, we take the median flux value of pixels along the boundary of a core as representing the constant background level of underlying layers of structure, and subtract that value from every pixel lying within the core. We refer to this as the background-subtracted total flux (and mass), and include the background-subtracted flux in Table 4. This background subtraction method will overestimate the contribution of larger-scale emission, particularly in the more clustered parts of the cloud, and therefore provides a strict lower limit to the dense core masses.

Figure 8 shows the cumulative mass functions measured from the total and background subtracted fluxes for the starless core population in each of the three regions observed (top row and bottom left panel), and also as a combined sample (bottom right panel). We omit the protostellar cores on the basis that their masses are more likely to be over-estimated by assuming a constant temperature of 20 K. We estimate the completeness level from a flux level of 3 σ across an area equal to the median starless core size. At the higher-mass end of the distribution, the slope is roughly consistent with the canonical Salpeter IMF (Salpeter 1955), for either estimate of the dense core masses. This similarity of the slope with the Salpeter IMF agrees with the original SCUBA analysis of Motte et al. (2001), and the combined SCUBA Orion A and B results of Nutter & Ward-Thompson (2007), among others. Although the *Herschel* core mass distribution for Orion B is not yet available for a direct comparison (see, however, Schneider et al. 2013, for the Orion B column density PDF), other star-forming regions tend to follow a similar profile (see, e.g., André et al. 2014).

At the very highest masses, we appear to have a slight deficit of starless cores relative to a pure Salpeter distribution. For example, extrapolating the mass function shown in black from around 1 Jy (around 1 M$_\odot$) up to 10 Jy using a Salpeter slope implies that there should be roughly three cores with total fluxes above 10 Jy, whereas our sample contains only one. The discrepancy between the Salpeter slope and the observed distribution of cores becomes even larger when the background subtracted masses are used instead. Both, however, are consistent within 3 σ Poisson uncertainties. An even larger sample of dense cores, ideally at least ten times more cores with high masses, would be needed to confirm whether or not this result is statistically significant. An absence of massive dense starless cores might be partially attributable to the tendency of object-identification algorithms to split large sources into multiple components. A real dearth of the most massive starless cores might also be partially attributable to a slightly higher detection rate of protostars in the infrared; since massive cores tend to have higher densities, it is possible that their natal protostars would tend to have higher accretion rates, and therefore

[37] While the maps at each *Herschel* wavelength analyzed by Schneider et al. (2013) are publicly released, the derived temperature and column density maps are not similarly available at present. A full re-derivation of the dust temperature across Orion B based on the *Herschel* data is beyond the scope of our present analysis.

higher luminosities. A larger sample size, combined with a detailed consideration of the typical accretion rates derived for detected protostars, would be necessary to test this scenario.

4.2. *Core Stability*

Using the sizes and estimated masses of all the dense cores, we can determine which cores are stable to gravitational collapse. Figure 9 shows the core masses and radii for all three regions, as indicated by the different colours. The JCMT effective beam width and the approximate flux sensitivity, i.e., three times the median noise level integrated across a given area are also shown. Our core selection criterion is slightly more complex than can be captured by a single completeness level. In particular, we removed sources that failed several local signal-to-noise ratio criteria, which are more stringent than the global level indicated. In Figure 9, we show masses derived from the total fluxes of all cores (left panel), as well as masses derived from background- subtracted total fluxes (right panel). The background-subtracted mass estimates tend to be smaller (as expected), and can be significantly smaller than our nominal total mass completeness level. We emphasize that our simple method for estimating the background level overestimates the true core background, likely by a significant amount for cores in crowded regions, and therefore those results should be treated with caution.

Assuming a spherical geometry for the dense cores allows us to estimate their mean densities. Lines of constant density of 10^4 cm^{-3}, 10^5 cm^{-3}, and 10^6 cm^{-3} are plotted in Figure 9. Most of the cores in the left panel lie between 10^4 cm^{-3} and several 10^5 cm^{-3}. Although not explicitly calculated there, the range spanned by our more massive dense cores is similar to that inferred from Figure 5 of Johnstone et al. (2001) and Figure 7 of Johnstone et al. (2006). Motte et al. (2001) use a wavelet-based source-finder and include deconvolution of the telescope beam in their final size measurement, which tends to lead to smaller sizes (and therefore higher mean densities) than we report. We also compared our results to those we would obtain using core sizes deconvolved by the telescope beam. Deconvolution had little effect most cores, since the majority of cores that we identify are significantly larger than the beam.

In Figure 9, we also plot the locus of Jeans mass for each radius for an assumed temperature of 20 K. Dense cores above the Jeans mass locus are expected to be unstable to collapse if thermal pressure provides the only avenue of support against gravitational collapse, and indeed, the majority of cores in this regime are associated with a protostar (of 33 cores in the unstable regime, 24 are protostellar), although we caution that the protostellar masses may be overestimated. Using instead the background-subtracted mass decreases the already small number of cores which lie above the Jeans instability line (17 unstable cores, of which 15 are protostellar). Johnstone et al. (2001) and Johnstone et al. (2006) similarly found that most dense cores lie within the range of stable Bonnor-Ebert sphere models (an equilibrium isothermal sphere model; Ebert 1955; Bonnor 1956). In addition, cores above this range tended to have high central concentrations, which are correlated with the presence of protostars (see discussion in the following section). Motte et al. (2001), however, argued that most of their identified dense cores were gravitationally unstable, with this difference being directly attributable to their smaller core size measurements obtained using a wavelet-based technique.

The inclusion of velocity information from a dense gas tracer is important to determine the role of turbulent motions in offsetting gravitational instability. While primarily sensitive to more diffuse gas than our SCUBA-2 observations, HARP ^{13}CO and C^{18}O observations of NGC 2023/2024 and NGC 2068/2071 show typical line widths of 1 – 3 km s^{-1} (Buckle et al. 2010), suggesting that some level of non-thermal support is likely present in the Orion B dense cores. With observations of a dense gas tracer such as N_2H^+, a more detailed consideration can be made of the level of non-thermal support present for each dense core (e.g., Kirk et al. 2007; Pattle et al. 2015). While non-thermal support mechanisms can explain the presence of starless cores lying above the Jeans stability line, it is harder to understand the presence of protostellar cores which appear to be Jeans stable. The most likely possibility is that the core boundaries we use in our analysis encompass both a smaller-scale unstable region where the protostar has formed and a larger-scale zone around it which is still stable, therefore making the core as a whole to appear to be stable.

4.3. *Concentration*

We measure the central concentration of each dense core as:

$$C = 1 - \frac{1.13 B^2 S_{850}}{\pi R_{eff}^2 F_{850}} \tag{4}$$

following Johnstone et al. (2001), where B is the effective beam width (in arcsec), S_{850} is the total flux (in Jy), R_{eff} is the effective radius (in arcsec; see Section 3 for the definition of R_{eff}), and F_{850} is the peak flux (in Jy bm^{-1}). For dense cores that are well-approximated by the Bonnor-Ebert sphere model, those having concentrations above 0.72 would be unstable to gravitational collapse (Johnstone et al. 2001). Previous work (Jørgensen et al. 2007, 2008; van Kempen et al. 2009) has also shown that highly concentrated dense cores tend to be associated with protostars.

In Figure 10, we show the concentration of the dense cores compared with their masses and effective radii. The top panel shows that the majority of protostellar cores have high concentrations that are normally taken to indicate gravitational instability (42 protostellar cores, versus 23 at lower concentrations). The starless cores have a much tighter distribution of concentrations around a value of ~ 0.72, which a two-sided KS test shows is statistically distinct, with a probability of 3×10^{-10} that the protostellar and starless core concentrations were drawn from the same parent sample. We note that some of the cores are elongated, complicating both the application of the Bonnor-Ebert sphere model and the interpretation of the concentration measurement. FellWalker does not calculate core elongations, since it does not fit any predetermined shape to the cores. We use the ratio of the 'size' of the core along the horizontal and vertical axes, each defined as the flux-weighted standard deviation of core pixel values from the flux-weighted centre position,

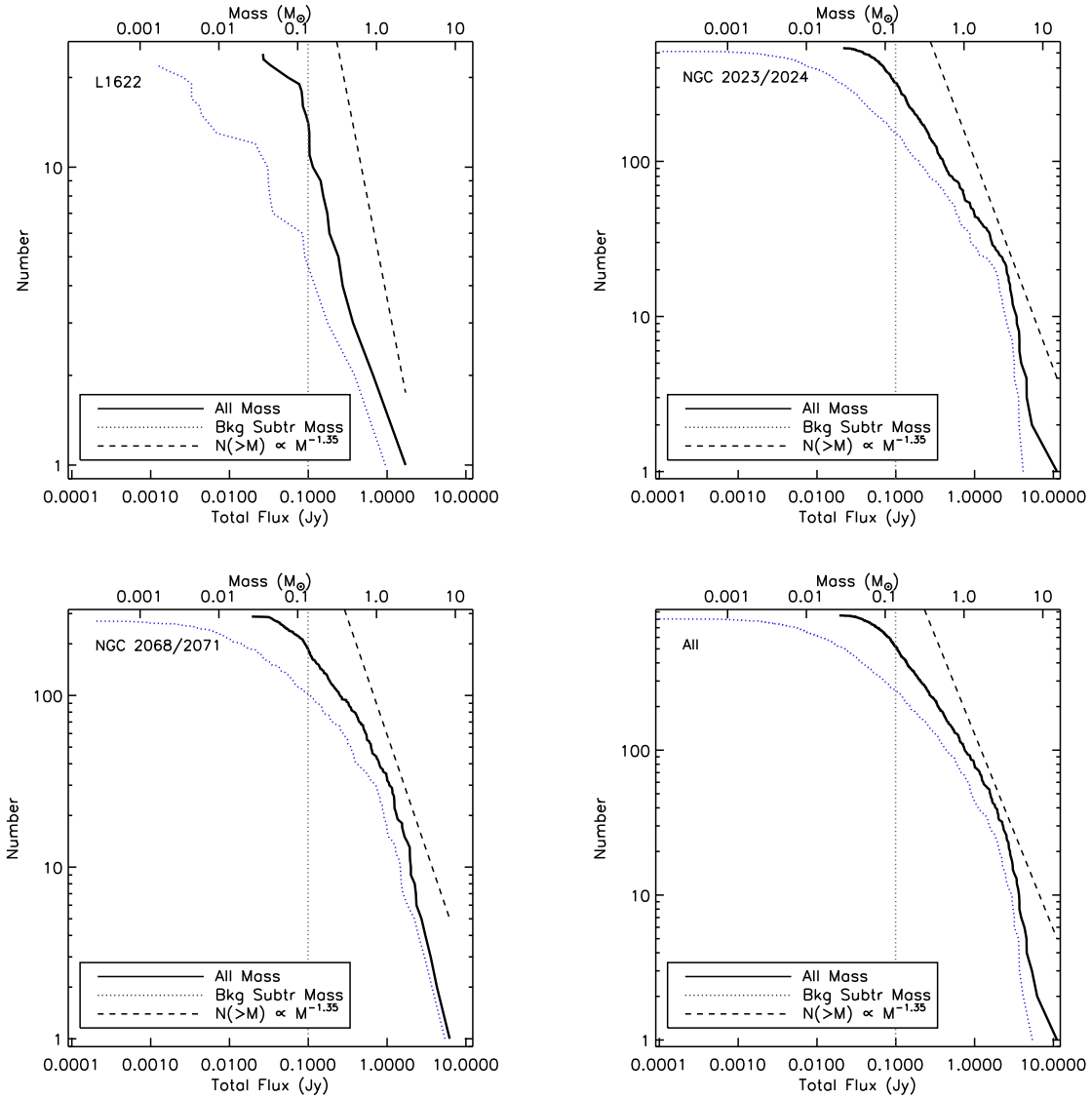

Figure 8. Cumulative mass functions for starless dense cores in L1622 (top left), NGC 2023/2024 (top right), NGC 2068/2071 (bottom left), and all three regions combined (bottom right). The black solid line shows the dense core masses using the full FellWalker-estimated masses, while the dotted blue line shows the background-subtracted masses. The dashed line shows a Salpeter slope of $N \propto M^{-1.35}$. The vertical grey line in the bottom right panel shows the completeness level. The bottom horizontal axis in all plots shows the total flux measured, while the upper axis shows the approximate mass, as estimated by a simple constant conversion factor (see text for details).

as a rough proxy for core elongation. With this measure, only 12% of the cores are elongated (ratios of 2 or higher), and they have a similar distribution of concentrations and effective radii to the other cores, so they do not bias the global distribution.

Lower concentrations for protostellar cores could indicate more evolved sources (c.f. van Kempen et al. 2009). SCUBA-2 is insensitive to the mass contained within the central protostar itself, so a protostar which has accreted much of the mass in its envelope would tend to have a lower concentration (see Mairs et al. 2014, for a discussion of protostellar mass versus 'envelope' mass in the context of comparisons with numerical simulations). The protostellar cores which lie the furthest below the thermal Jeans line, and those with smaller total masses both tend to have lower concentrations as well, which supports this hypothesis.

In contrast to prior work, we find that a significant number of starless dense cores have high concentrations that would nominally indicate instability (299 starless cores have concentrations above 0.72 while 551 have lower concentrations). At least some of these higher values of concentrations are likely attributable to the increased sensitivity of SCUBA-2 compared with SCUBA. Johnstone et al. (2003) and Johnstone et al. (2006) find a range of concentrations from about 0.3 to 0.9 for dense cores in Orion B using SCUBA data, whereas our concentration measurements range between roughly 0.5 and 0.95. Since the resolution of SCUBA and SCUBA-2 are identical, these differences must be attributable to the improved sensitivity of SCUBA-2 data and possibly also the core identification algorithm used (ClumpFind versus FellWalker). FellWalker, like ClumpFind, tends to include lower flux material around peaks within the bound-

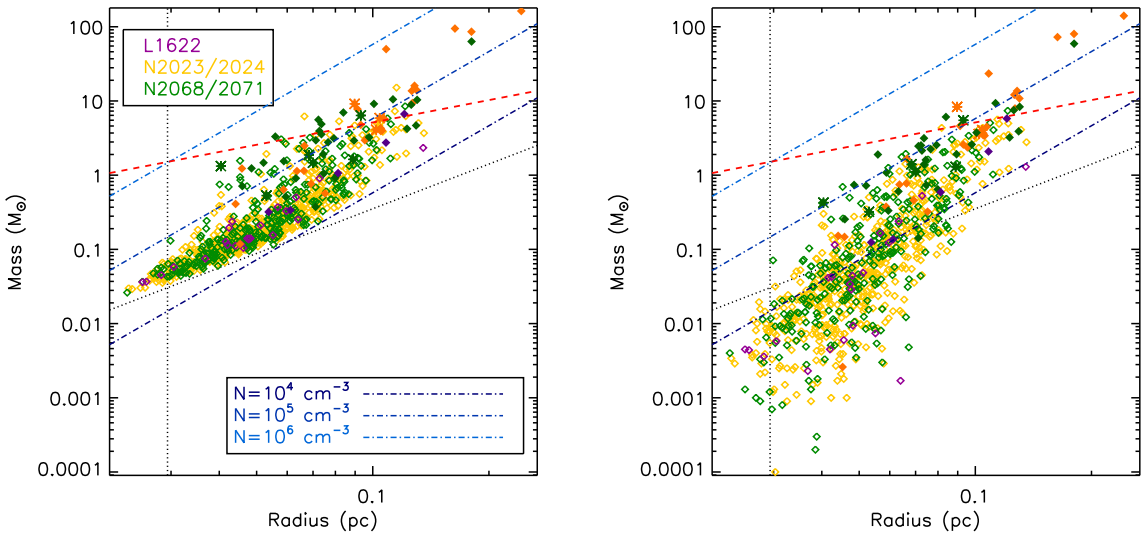

Figure 9. Distribution of dense core masses and sizes for each region observed. The colours indicate the region observed: L1622 (purple), NGC 2023/2024 (yellow), and NGC 2068/2071 (green), while the open diamonds indicate starless cores and the filled diamonds indicate protostellar cores. The protostars have a slightly darker shading to enable better visibility, and the deeply embedded protostars from Stutz et al. (2013) are denoted by asterisks. The dotted lines denote the approximate sensitivity levels (the vertical line shows the beamwidth, while the diagonal line shows 3 times the typical rms integrated over a given radius). The blue diagonal dash-dotted lines show the relationship expected for constant (3D) density objects, ranging from 10^4 cm^{-3} to 10^6 cm^{-3} from dark to light (bottom to top). The dashed diagonal red line shows the locus of Jeans masses for a temperature of 20 K. The left panel indicates the total mass within each core, while the right panel indicates the background-subtracted mass within each core. See text for details.

ary of a core. Thus, cores identified in higher sensitivity observations will tend to have larger sizes and total fluxes, with the core area increasing faster than the total flux (since only faint pixels are being added). We therefore expect that the increased sensitivity of the SCUBA-2 observations, coupled with the improved recovery of larger-scale emission, will increase the concentrations of our cores relative to similar analyses of SCUBA observations. At the same time, cores with larger areas relative to their fluxes (or masses) will appear more stable in the mass versus radius analysis shown in Figure 9.

4.4. *Dense Cores and Ambient Cloud Pressure*

Lombardi et al. (2014) used a combination of *Planck* and *Herschel* data across Orion (A and B clouds) to estimate the total column density of material down to a resolution of 36″ in areas with *Herschel* coverage. We use this map, including Lombardi et al.'s recommended scalings between optical depth at 850 μm and total column density, to compare with the SCUBA-2 dense cores. L1622 falls outside of the Lombardi et al. (2014) column density map, and so is not included in this analysis. Previous analyses (e.g., Onishi et al. 1998; Johnstone et al. 2004; Hatchell et al. 2005; Kirk et al. 2006; Enoch et al. 2006, 2007; Könyves et al. 2013) have shown that dense cores tend to be found in regions of higher overall column density, although historically these analyses have relied on much lower resolution measurements of the overall cloud column density.

Under the assumption that a molecular cloud is a sphere, the column density at a given location within the cloud can be used as a proxy for the external pressure due to the overlying weight of the cloud. In this simple model, a higher local column density implies a three dimensional position closer to the cloud centre, and hence a larger weight of overlying cloud material. While the Lombardi et al. (2014) column density map clearly shows that the Orion B cloud is more complex than a sphere, the spherical assumption provides a practical method to estimate the bounding pressure on dense cores due to the ambient cloud material. Furthermore, the model's implication that sources in higher column density zones are likely surrounded by more material than those in lower column density zones seems generally reasonable. Following McKee (1989), and the implementation in Kirk et al. (2006), the pressure at depth r in a cloud is given by

$$P(r) \simeq \pi G \bar{\Sigma} \Sigma(r) \tag{5}$$

where $\bar{\Sigma}$ is the mean column density and $\Sigma(r)$ is the column density measured at cloud depth r. For cores near the cloud centre, the column density along the line of sight to the core is roughly twice this value, i.e., $\Sigma_{obs} = 2 \times \Sigma(r)$. In both NGC 2023/2024 and NGC 2068/2071, the mean cloud column density over the area observed by SCUBA-2 is $9{\times}10^{21}$ cm^{-2}. For each core, we measure the local cloud column density as the maximum value of the Lombardi et al. (2014) column density map within the core's footprint (there are typically only a few resolution elements within each core footprint). If we make the assumption that the cores can be well represented by an isothermal sphere model, the critical radius and mass of each core can be written as

$$R_{crit} = 0.49 \frac{c_s^2}{\sqrt{GP}} \tag{6}$$

and

$$M_{crit} = c_s^4 \sqrt{\frac{1.4}{G^3 P}} \tag{7}$$

where c_s is the sound speed and G the gravitational constant (equations adapted from Hartmann 1998). In

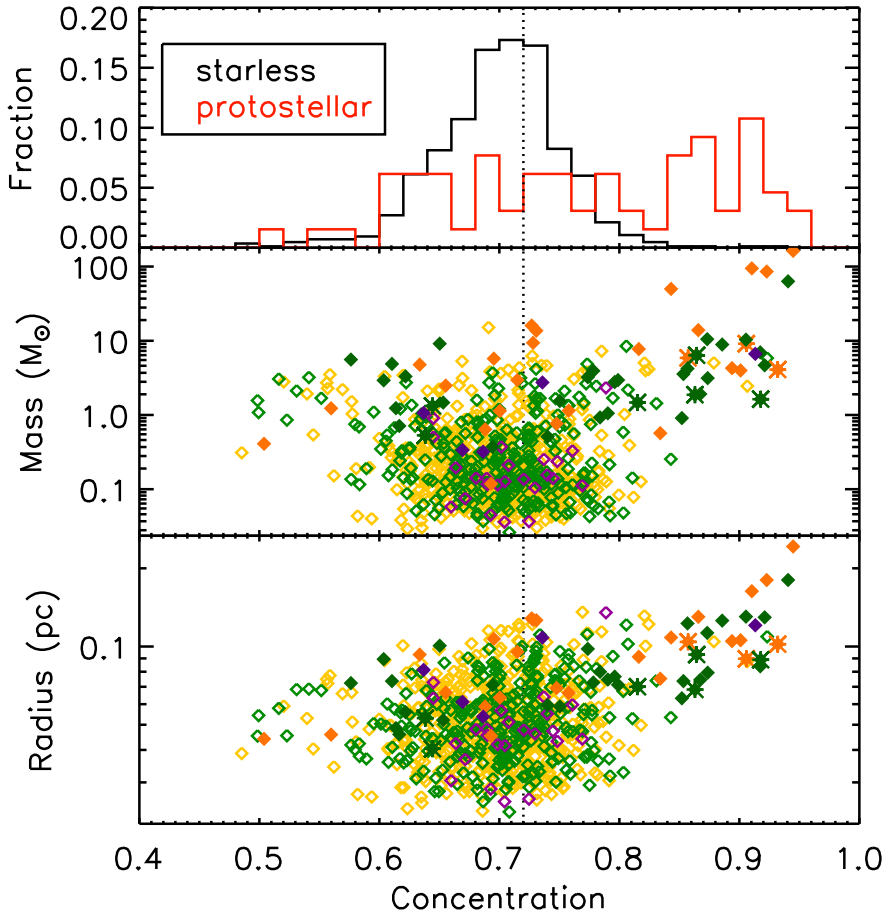

Figure 10. The distribution of dense core concentrations (top panel) compared with their estimated masses (middle panel), and effective radii (bottom panel). The red line in the top panel and filled diamonds in the bottom two panels indicate dense cores associated with a protostar, with the deeply embedded protostars from Stutz et al. (2013) shown in asterisks, while the black line in the top panel and the open diamonds in the bottom two panels indicate starless cores. Cores with concentrations above 0.72 (vertical dotted line) would be gravitationally unstable under a Bonnor-Ebert sphere model.

Figure 11, we show the relationship between core sizes and masses and the total cloud column density at the core positions. We see a strong correlation between the cloud column density and the core masses, and a weak correlation between the cloud column density and the core sizes, in contrast with Sadavoy et al. (2010), who compared SCUBA-based dense core properties with extinction-based column density measures in five nearby molecular clouds, including Orion. Given the large scatter in the relationships that we observe, we expect the discrepancy with Sadavoy et al. (2010) is the result of the much larger number of dense cores in our present analysis, and the larger parameter space that they occupy.

With the pressure of the overlying cloud material estimated using the spherical-cloud assumption discussed above, many of the cores have sizes and masses larger than can be thermally supported given this external weight of the cloud. By size, all protostars and 522 of 826 starless cores lie above the critical value, while by mass, 50 of 60 protostars and 101 of 826 starless cores lie above the critical value (note that cores in L1622 are not included in this analysis). The fraction of cores deemed unstable by this simple pressure analysis is a significant change from the apparent thermal stability of the dense cores seen in Figure 9 (24 of 60 protostellar cores lie above the thermal Jeans mass compared to 9 of 826 starless cores; see Section 4.2) and shows that the pressure from the ambient molecular cloud plays a strong role dense core stability. A similar result has been seen in other dense core analyses (e.g., Kirk et al. 2007; Lada et al. 2008; Pattle et al. 2015). Beyond stability considerations from a hydrostatic equilibrium model, non-thermal forces may be contributing significantly to the pressure on individual cores, which might help to explain the large scatter apparent in Figure 11.

While we identify dense cores inhabiting a wide range of cloud column densities, we note that the correlation between the cores' size or mass with the cloud column density also implies that there is a minimum column density value at which pressure-unstable cores are found. This minimum column density is approximately 10^{22} cm^{-2}, which is somewhat higher than the column density threshold observed in nearby star-forming regions, which is usually around 5-7$\times10^{21}$ cm^{-2} (e.g., Onishi et al. 1998; Johnstone et al. 2004; Kirk et al. 2006; Enoch et al. 2006, 2007; Könyves et al. 2013).

4.5. *Cloud Structure and Core Lifetimes*

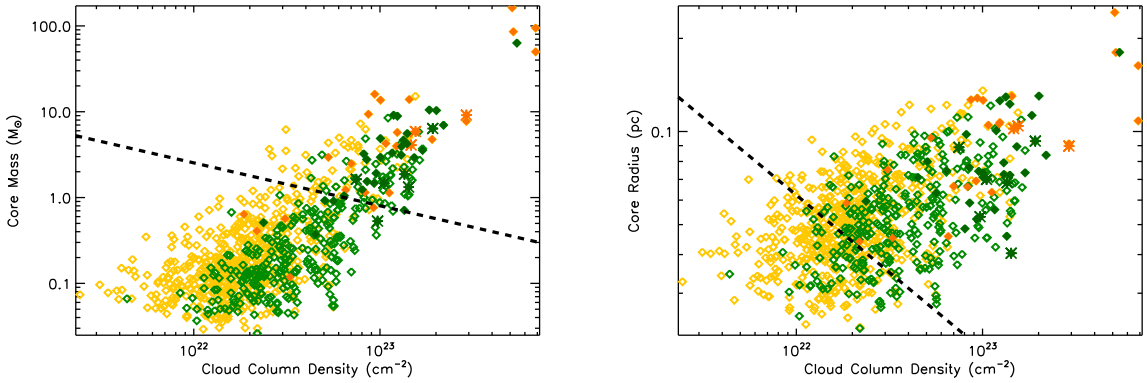

Figure 11. Dense core sizes (left) and masses (right) compared to the local cloud column density from Lombardi et al. (2014). The colour scheme follows Figure 9, i.e., NGC 2023/2024 cores are plotted as yellow/orange diamonds, while NGC 2068/2071 cores are plotted as green / dark green diamonds. The darker, filled diamonds indicate protostellar cores, and the asterisks denote the protostars from Stutz et al. (2013). In both panels, the dashed black line shows the critical radius (left) and mass (right) for an isothermal sphere model at 20 K with an external pressure derived from the local cloud column density. Most of the protostellar cores lie above the line of critical stability.

In Figure 12, we compare the cumulative mass fractions of dense cores (using the total mass estimated) and cloud mass as functions of the cloud column density from Lombardi et al. (2014) for NGC 2023/2024 and NGC 2068/2071. For a fair comparison between the dense core mass and cloud mass fractions, we consider only areas observed with SCUBA-2. For the dense cores, we take the column density at each pixel that lies within a dense core footprint (excluding other pixels as noise). Figure 12 shows that the dense cores seen by SCUBA-2 are associated with the highest column density material. For example, roughly 24% and 43% of the mass in SCUBA-2 cores in NGC 2023/2024 and NGC 2068/2071 respectively is associated with total column densities above 10^{23} cm^{-2}, whereas only a small fraction of the cloud material (3% and 5% respectively) lies within this range. We also compare in Figure 12 the protostar number fraction with the column density at the locations of protostars from Megeath et al. (2012) and Stutz et al. (2013). Assuming that all protostars have similar masses, the fractional number of protostars within a column density contour is equivalent to their fractional mass within that same contour. We find that the protostars are also concentrated in regions of high column density, although slightly less so than the dense cores in NGC 2068/2071. Since the protostellar list from Megeath et al. (2012) likely includes some slightly older protostars that have drifted from their birthsites, it is not surprising for a YSO population to have a slightly wider range of column densities than the dense cores.

We can also consider the above distributions in terms of total masses, as shown in Figure 13. The total mass in NGC 2023/2024 and NGC 2068/2071 within the areas observed by SCUBA-2 is 10600 M$_\odot$ and 9000 M$_\odot$, respectively, while the total mass in dense cores is 780 M$_\odot$ and 340 M$_\odot$, respectively. Again, we emphasize that the dense core masses are estimated assuming a constant temperature of 20 K. Both NGC 2023/2024 and NGC 2068/2071 have several large and massive protostellar dense cores for which this assumption will cause the mass to be overestimated. These particular dense cores are coincident with the highest total column densities in the Lombardi et al. (2014) map, which is responsible for making the total dense core mass strangely appear larger than the total gas and dust mass at the highest column densities in Figure 13. It is also likely that, due to their slightly lower resolution (compared to SCUBA-2), Lombardi et al. (2014) may slightly underestimate the total mass in the highest column density and smallest scale structures. Even with these caveats, it is interesting to note that above $1-2\times10^{23}$ cm^{-2}, nearly all of the high column density material is already in dense cores. Below this column density, the dense cores represent an ever-decreasing fraction of the total mass.

At the highest column densities, 10-20% of the dense core material is already located within protostars, if we make the assumption that each protostar has a mass of 0.5 M$_\odot$. At lower column densities, the mass in YSOs is only around 6% of the dense core mass in NGC 2023/2024 while it is 16 – 22% in NGC 2068/2071. In both regions, the mass within YSOs is less than 1% of the total cloud mass. There is no indication of a strong relationship between the total column density and the ratio of YSO mass to dense core mass, though it is possible that systematic biases in our simple mass estimations which hide such a trend (e.g., if YSOs tend to be more massive in high column density environments). At lower column densities, the ratio of YSO mass to dense core mass in NGC 2023/2024 is roughly a factor of 4 lower than in NGC 2068/2071. This result could imply that NGC 2023/2024 is younger, and that the protostars there have only started to form recently. Although the total numbers of sources are small, Stutz et al. (2013) also found a higher proportion of the youngest protostellar candidates ("PBRs") in NGC 2023/2024 than in NGC 2068/2071 relative to YSOs found in the *Spitzer*-based catalogue of Megeath et al. (2012). This result also supports the scenario of NGC 2023/2024 being younger, as does the relatively larger percentage of YSOs that we see at lower column densities in NGC 2068/2071 (Figure 12).

The ratio of starless cores to protostellar cores has also been used as a tool to estimate the relative lifetimes of the two stages, with the estimated protostellar lifetime then used as an anchor to obtain absolute lifetimes. Previous analyses of dense cores detected with SCUBA and similar instruments have suggested lifetimes of both to be several tenths of a Myr, with a similar number of protostel-

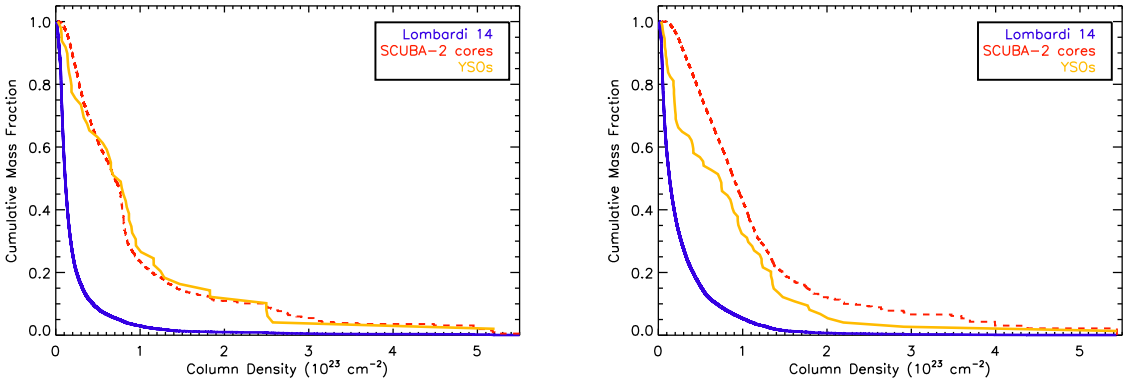

Figure 12. A comparison of the cumulative mass fraction within SCUBA-2 cores and the entire cloud of gas and dust as measured by Lombardi et al. (2014) across NGC 2023/2024 (left panel) and NGC 2068/2071 (right panel). In each panel, the solid blue line shows the fraction of mass at a given column density or higher within the area observed by SCUBA-2, while the dashed red line shows the fraction of mass in dense cores. The yellow line shows the fraction of protostars from Megeath et al. (2012) and Stutz et al. (2013) at the same column density or above.

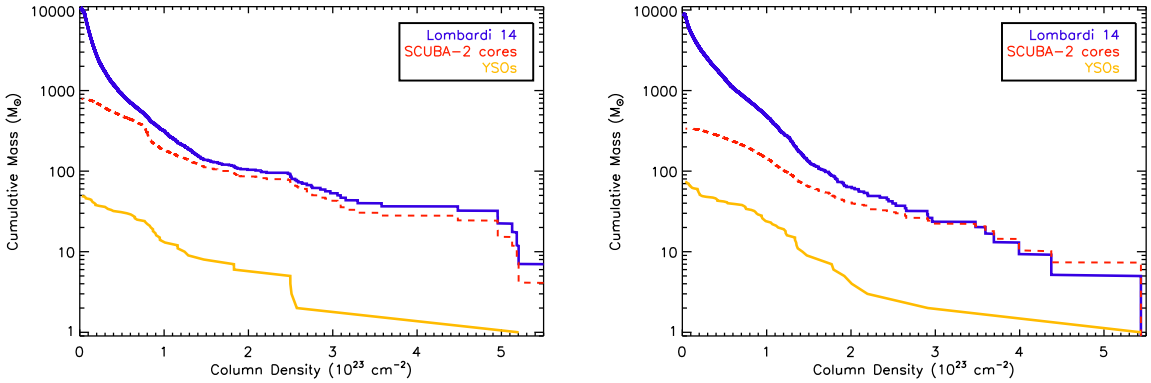

Figure 13. A comparison of the cumulative mass within SCUBA-2 cores and the entire gas and dust mass as measured by Lombardi et al. (2014) across NGC 2023/2024 (left panel) and NGC 2068/2071 (right panel). In each panel, the solid blue line shows the total mass at a given column density or higher within the area observed by SCUBA-2, while the dashed red line shows the total mass in dense cores (see Section 4.1 for the assumptions used). The yellow line shows the mass in protostars, assuming they each have a mass of 0.5 $M_\odot$.

lar and starless cores identified (e.g., Enoch et al. 2008; Hatchell et al. 2007; Kirk et al. 2005), while earlier analyses, such as that of Jessop & Ward-Thompson (2000) suggested the starless core lifetime decreases with the core's volume density. With our more sensitive census of cores detected with SCUBA-2, we identify a much larger population of starless dense cores, and can re-visit this question, although we caution that examining only cores within a single cloud may introduce some bias. Furthermore, some of the dense cores in our sample may be transient features which never evolve to form a star. In our full sample, we have 851 starless cores and 64 protostellar cores, i.e., a ratio of 13:1. If we sub-divide the dense cores into bins of varying mean density, we find a roughly 1:1 ratio for starless to protostellar cores above mean densities of 10^5 cm^{-3}, and a rapidly increasing ratio beyond that, as shown in Table 2. In Table 2, we include the ratio of protostellar cores for both the full dense core sample, as well as when the cores are restricted to those more massive than 0.1 $M_\odot$ (i.e., those which presently have sufficient mass to form a star and may therefore be less likely to be transient features). While the protostellar ratios differ in the lower density bins, depending on which sample is examined, both show the same trend of a protostellar ratio which decreases rapidly with protostar density. This result is qualitatively in agreement with Jessop & Ward-Thompson (2000) in that dense core lifetimes do indeed appear to be longer for cores with lower mean density. We caution, however, that our assumption of a constant temperature tends to bias the protostellar core masses (and hence mean densities) to higher values, which would therefore serve to increase the fraction of protostellar cores in the higher density bins from their true value. Similarly, if some starless cores were colder than 20 K, their masses and densities would be *under*estimated which would increase the number of starless cores in the higher density bins.

The concentration measured for each core is likely to be less biased by a non-constant temperature than density / mass estimates are. Separating the dense cores into those with high and low concentrations (above and below the nominal maximum stable value of 0.72) shows that more concentrated dense cores are more likely to be protostellar. The starless to protostellar core ratio for high concentrations is 7:1 (299 versus 42) while the ratio for low concentrations is 24:1 (551 versus 23). We note that these ratios are very similar when only dense cores more massive than 0.1 $M_\odot$ are considered: there,

Table 2
Ratio of Starless to Protostellar Cores

Density Range[a] (cm^{-3})	All Cores[b]			Cores > 0.1 $M_\odot$[c]		
	N_{sl}	N_p	Ratio	N_{sl}	N_p	Ratio
$> 10^5$	34	31	1:1	34	31	1:1
$10^{4.5} - 10^5$	270	29	9:1	205	29	7:1
$10^4 - 10^{4.5}$	546	5	109:1	392	5	78:1

[a] Mean core densities calculated using the total mass and effective radius.
[b] Number of starless cores, protostellar cores, and their ratio for the full dense core sample.
[c] Number of starless cores, protostellar cores, and their ratio for dense cores above 0.1 $M_\odot$.

the ratios are 6:1 and 22:1, respectively.

Both the concentration and mean density results support the simple picture that as dense cores evolve, they tend to become denser and more centrally concentrated before they are able to form a protostar.

5. DISCUSSION

Lada et al. (1991) identified roughly 300 YSOs in each of the NGC 2023/2024 and NGC 2068/2071 regions, corresponding to an additional 150 $M_\odot$ for each region beyond the YSO masses discussed in the previous section. With an efficiency of converting dense core mass into YSOs of 30%, approximately 235 $M_\odot$ and 100 $M_\odot$ of YSOs in NGC 2023/2024 and NGC 2068/2071, respectively, may be created from the current population of dense cores. This number would roughly double the existing stellar populations in both regions, and is several times larger than the existing YSO population in either region. The total amount of mass at lower densities in each region is around 10000 $M_\odot$; if even 1% of this mass ends up also contributing to future stars, it would contribute about the same amount of stars again. Both of these regions therefore may one day harbour stellar clusters containing many hundreds of stars. At the present star formation rate, it will take several million years to deplete the current population of dense cores. Since the most massive dense starless cores present reach only about 10 $M_\odot$, it is likely that B stars will be the most massive that can eventually form and help to drive the dissipation of the remaining cloud material.

L1622 appears to have less material available to form additional YSOs with a total dense core mass of 18 $M_\odot$ and roughly 6 $M_\odot$ presently in YSOs. The total cloud mass cannot be estimated to the same precision as NGC 2023/2024 and NGC 2068/2071 since a full column density map is not presently available. Based on the CO maps of Maddalena et al. (1986), however, L1622 appears to be a factor of at least several less massive than NGC 2023/2024 or NGC 2068/2071. This too suggests that a limited amount of star formation may occur in the future in L1622. As outlined in the introduction, the distance to L1622 is less certain, and some observations suggest a distance of < 200 pc (see discussion in Reipurth et al. 2008). If this closer distance is indeed correct, then L1622 would be an even more quiescent region than our analysis here suggests. For example, all of the core sizes would increase by a factor of ~ 2, while the masses would decrease by a factor of ~ 4. Also, the shorter distance would push all of the cores below the thermal Jeans line in Figure 9, while the cores' concentrations would remain unchanged. Since L1622 cores represent a small fraction of the total core population analyzed here, there would be minimal impact on our overall conclusions.

6. CONCLUSION

We have presented a first-look analysis of SCUBA-2 observations of the Orion B molecular cloud taken as part of the JCMT Gould Belt Survey. The improved sensitivity and larger detector size of SCUBA-2 compared to SCUBA has allowed for significantly larger and more sensitive maps, with these SCUBA-2 observations reaching an rms of 3.7 mJy bm^{-1}, four to six times lower than previous SCUBA observations. Approximately 0.6, 2.1, and 1.7 square degrees were mapped in L1622, NGC 2023/2024, and NGC 2068/2071, respectively. In addition to the catalogues presented here, all of the reduced datasets analyzed in this paper (850 μm and 450 μm emission maps, the CO-subtracted 850 μm map, and the 850 μm-based FellWalker core footprint, along with maps of the variance per pixel, and the external mask applied) are available at `https://doi.org/10.11570/16.0003`.

We used the FellWalker algorithm to identify 915 dense cores within the 850 μm map, and analyzed their basic properties. Protostellar dense cores are identified through association with a protostar in the *Spitzer* (Megeath et al. 2012) or *Herschel* (Stutz et al. 2013) catalogues. Assuming a constant temperature of 20 K yields a starless core mass function similar to that derived in other studies, with the high-mass end following a roughly Salpeter slope. Comparing the core masses and radii showed that most cores have mean densities between 10^4 cm^{-3} and several 10^5 cm^{-3}. Dense cores with masses above the thermal Jeans mass for the assumed temperature of 20 K tend to be protostellar, although there are both starless cores and protostars on both sides of this relationship. A larger number of cores appear to be unstable when the bounding pressure due to the weight of the overlying cloud material is accounted for. We measure a range of central concentrations for the dense cores which tends to have larger values than previous SCUBA analyses (Johnstone et al. 2003, 2006), which we speculate is due to our deeper sensitivity. At the highest mean densities, the lifetimes of the starless and protostellar stages of dense cores appear to be fairly similar, consistent with previous observations, while the least dense cores in our sample may be longer-lived entities, if they are destined to form stars at all. Comparison of the distribution of dense cores we identified to the overall cloud column densities in NGC 2023/2024 and NGC 2068/2071 measured by Lombardi et al. (2014) shows that at high column densities, above $1 - 2 \times 10^{23}$ cm^{-2}, nearly all of the material is contained in the dense cores, while at lower cloud column densities, dense cores comprise a much smaller fraction of the material. Based on the amount of dense gas available, we predict that each of NGC 2023/2024 and NGC 2068/2071 will form at least as many stars as are currently present, while L1622 has little dense material available to supplement the present-day small protostellar population. We will present an in-depth analysis of the clustering properties of the dense cores in Kirk et al (2015, in prep).

APPENDIX

DENSE CORE IDENTIFICATION

Here, we describe our identification of dense cores, which was based on Starlink's Fellwalker algorithm (Berry 2015). The FellWalker algorithm is based on the idea of hiking through a set of hills: peaks are defined as local maxima, with their extents based on the routes that a hiker could ascend to reach the top of each peak. Users can set parameters in the algorithm such as the minimum peak size, minimum dip between neighbouring peaks, minimum ascent slope, etc. Prior to running FellWalker, we made a qualitative comparison between our 850 μm maps and the publicly available *Herschel* 500 μm map (Schneider et al. 2013). This comparison revealed that surprisingly faint structures in the 850 μm map all have counterparts in the *Herschel* 500 μm data. Given this correspondence, we adopted less stringent FellWalker parameters than the default recommended values. In particular, the parameters we modified from the default values are:

- `FellWalker.AllowEdge = 0` *(eliminate objects touching a map edge)*
- `FellWalker.Noise = 0.5*RMS` *(extend object search deeper into the noise)*
- `FellWalker.MaxJump = 2.5` *(reduce area for identifying shared peaks)*
- `FellWalker.MinPix = 5` *(allow smaller objects to be identified)*
- `FellWalker.CleanIter = 5` *(tidy up jagged source edges)*

We then ran the FellWalker source list through a second program to eliminate spurious sources, which were numerous with the relaxed criteria above. Since the noise at the edges of the maps and mosaics is larger than in the centre, a large number of spurious sources were identified with FellWalker, which assumes a constant noise level across the map. We tested a variety of criteria to weed out spurious sources, and found the following set of criteria to be the most effective at removing noise sources while retaining real sources. We removed: 1) sources smaller than the effective beamsize, 2) sources which had fewer than three pixels above twice the local noise level, and 3) sources which, when slightly smoothed, had fewer than fifteen pixels above the local noise level. In addition, sources identified very near to the map edge (where the noise was highest) were eliminated if they had fewer than 22 pixels above the local noise level, when the image was slightly smoothed (i.e., 50% more pixels than the third criterion). All of the remaining sources passed our visual inspection. In general, the 3rd criterion eliminated the most sources. The first criterion almost never rejected any sources since FellWalker itself eliminates sources smaller than the beam. FellWalker identified 260, 1383, and 1020 sources in L1622, NGC 2023/2024, and NGC 2068/2071 respectively, which reduced to 29, 564, and 322 reliable cores after the cuts described above.

COMPARISON TO SCUBA

Parts of both the NGC 2023/2024 and NGC 2068/2071 regions were observed with the original SCUBA instrument, and analyses of these observations which include independently-derived core catalogues are given in Motte et al. (2001), Mitchell et al. (2001), Johnstone et al. (2001), Johnstone et al. (2006), Nutter & Ward-Thompson (2007), and Di Francesco et al. (2008). Both Nutter & Ward-Thompson (2007) (hereafter NWT07) and the SCUBA Legacy Catalog of Di Francesco et al. (2008) (hereafter SLC) include all observations taken during SCUBA's operation of Orion B, and so we use these two works to compare the sensitivity of SCUBA and SCUBA-2 in Orion B[38].

Figures 14 and 15 show the SCUBA-2 850 μm images of the portions of NGC 2023/2024 and NGC 2068/2071 that were covered by SCUBA, based on the 'coverage maps' from the SLC[39]. The left panels of Figures 14 and 15 show the cores listed in NWT07, while the right panels show the SLC cores. Since both NGC 2023/2024 and NGC 2068/2071 have clustered and complex emission, we expect differences to arise in core boundaries and the level of fragmentation. To compare the core catalogues quantitatively, we associate the peak position of each SCUBA core with the FellWalker core whose boundary it lies within. Indeed, Figures 14 and 15 show that all of the cores in NWT07 have a match in our SCUBA-2 core catalogue, while several of the SLC cores do not have a match. Table 3 shows the number of cores matched for each catalogue. Comparing the number of cores in the two SCUBA-based catalogues which do and do not have a match in the SCUBA-2 catalogue suggests that the SLC probes deeper than NWT07 in NGC 2023/2024 while the reverse is the case in NGC 2068/2071. In both cases, the SLC is more susceptible to falsely identifying cores. The SCUBA-2 catalogue includes several times more cores than seen with SCUBA over a comparable area: roughly 300 additional cores were found in the SCUBA-2 map of the part of NGC 2023/2024 observed with SCUBA (compared to 60-90 cores identified with SCUBA), while roughly 150 additional cores were found in NGC 2068/2071 (compared to 90-100 identified with SCUBA).

Figures 16 and 17 show comparisons of the peak fluxes, total fluxes, and sizes measured for cores in NGC 2023/2024 and NGC 2068/2071 respectively. The SCUBA Legacy maps were created with a resolution of 19.8″(Di Francesco et al. 2008), degraded from the nominal best value to better handle noise features in their processing of multiple datasets of differing quality. We roughly correct for differences expected in the SLC values caused by this lower resolution:

[38] For completeness, we note that one single small 'jiggle map' (pointed observation) was taken in the L1622 region, but given the small quantity of data, we do not make comparisons in this region.

[39] `http://www4.cadc-ccda.hia-iha.nrc-cnrc.gc.ca/community/scubalegacy/`

Table 3
Number of cores matched between SCUBA and SCUBA-2 maps

Region	NWT07[a]		SLC[b]		FW-NWT07[c]		FW-SLC[d]	
	match	no mat.	match	no mat.	match	no mat.	match	no mat.
NGC 2023/2024	59	0	90	9	57	312	80	291
NGC 2068/2071	100	0	87	2	90	147	80	157

[a] Number of cores in Nutter & Ward-Thompson (2007) which were and were not matched to a SCUBA-2 FellWalker core.
[b] Number of cores in the SCUBA Legacy Catalog (Di Francesco et al. 2008) which were and were not matched to a SCUBA-2 FellWalker core.
[c] Number of SCUBA-2 FellWalker cores associated with one or more cores in Nutter & Ward-Thompson (2007).
[d] Number of SCUBA-2 FellWalker cores associated with one or more cores in the SCUBA Legacy Catalog.

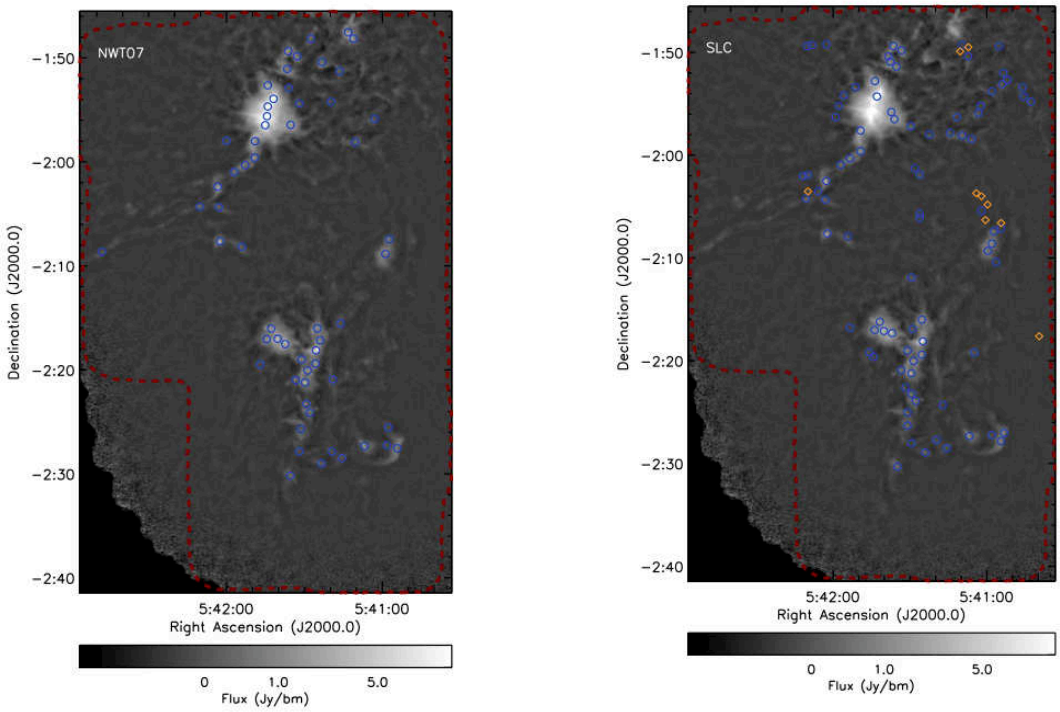

Figure 14. A comparison of cores identified with SCUBA and the present SCUBA-2 850 μm map in NGC 2023/2024. The greyscale in both panels shows the SCUBA-2 observations; the red dashed line indicates the area observed with SCUBA. The left panel shows the peak positions of NWT07 cores, while the right panel shows the SLC cores. In both panels, blue circles indicates cores which had a match in our SCUBA-2 catalogue, while orange diamonds indicate cores with no match in our catalogue (i.e., peak position outside of all SCUBA-2 FellWalker core footprints). All of the NWT07 cores had a match in NGC 2023/2024.

we decrease the SLC peak flux by the ratio of beam sizes, and deconvolve the SLC radius with the 19.8″ beam, and reconvolve it with the SCUBA-2 14.6″ beam (given typical core sizes, the radius correction tends to be very small). The NWT07 catalogue had a similar effective radius to our SCUBA-2 map, so corrections are not needed for that comparison. Most of the core catalogue values agree reasonably well between the two SCUBA measurements and the SCUBA-2 measurement, although there is significant scatter around a perfect one-to-one relationship. We expect the peak flux to show the best agreement, and indeed that is generally true. Note that the scatter in the comparison with the NWT07 peak fluxes is likely due to the lower precision of their published catalogue values, which were only given in tenths of a Jy bm^{-1}. Since generally cores become more numerous at lower flux levels (when above the detection limit), we expect that most of the cores shown at each of the several tenths of a Jy bm^{-1} level in peak flux would in fact have slightly lower true values, lowering the apparent scatter. The total flux and size plots tend to show a larger scatter between the SCUBA and SCUBA-2 values, as these measures are more sensitive to precisely how the dense core boundaries are defined, which tends to vary more between core identification methods in regions of complex emission. We do not see any indication of systematic calibration issues between the SCUBA and SCUBA-2 maps: the median ratio of peak or total flux in SCUBA and SCUBA-2 cores is not consistently higher or lower than one across both regions in the NWT07 or SLC catalogues.

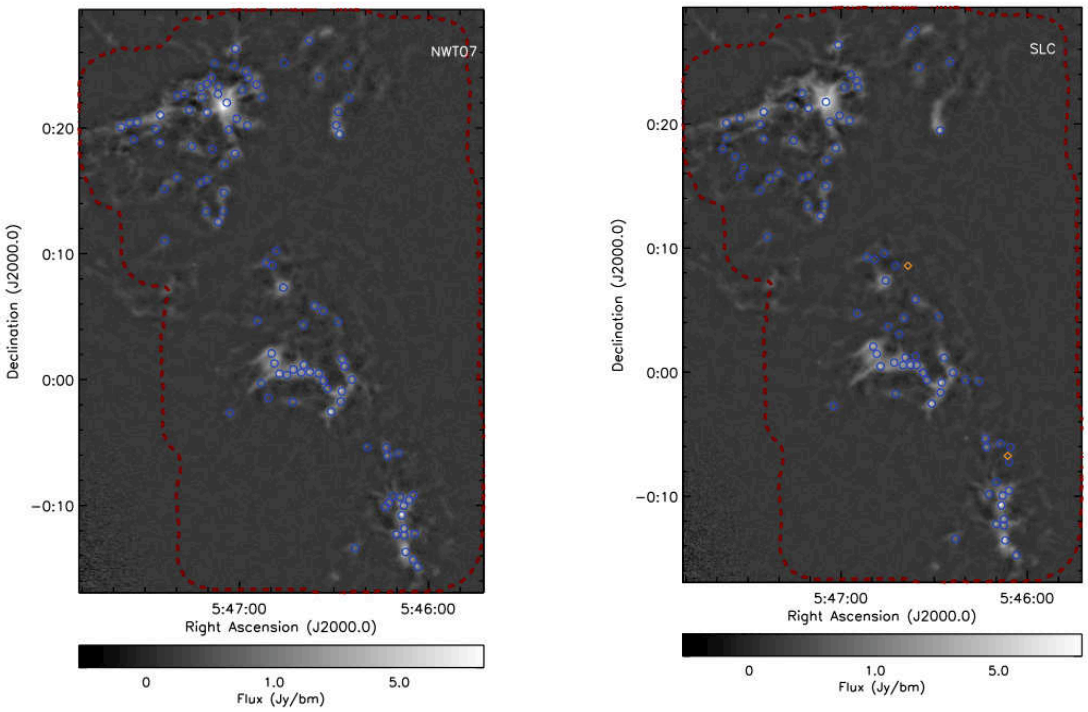

Figure 15. A comparison of cores identified with SCUBA and the present SCUBA-2 850 μm map in NGC 2068/2071. See Figure 14 for the plotting conventions used.

Barring the problem with the lower precision in the peak flux values given in NWT07, we find generally good agreement between the measured core properties from SCUBA-2 and those in NWT07 and the SLC. The SCUBA Legacy processed images have some negative features ("bowls") around bright cores. Also, the NGC 2023/2024 and NGC 2068/2071 regions happened to be split between two 'tiles' in the SLC dataset, which appears to have caused a particularly poor automated reduction of these regions. The resulting large scale bowls and pedestals make the resulting core catalogue less accurate. This difference likely acounts both for the large scatter away from the one-to-one relationship in the total flux comparison, as well the presence of SLC cores which have no match in our SCUBA-2 catalogue. Visual inspection of the SLC cores which are unmatched show they are either caused by noise spikes at map edges, or are small-scale noise features coincident with a large-scale pedestal that raised them above the global flux cutoff used.

For our comparison with the SLC, since the 850 μm maps and source boundaries are publicly available, we can explicitly also test the cause of the un-matched FellWalker sources. In Figure 18, we show the SCUBA Legacy flux at the position of each unmatched FellWalker core peak position. As can be seen in the figure, there is generally a good correspondence between the FellWalker core peak flux and the SCUBA Legacy flux at the same location. We additionally find that the majority of the brighter unmatched FellWalker cores have peak positions which lie within an SLC source boundary. In these cases, it is clear that the reason that the FellWalker core was unmatched is differences in source boundaries in regions of complex emission: the SLC source which the FellWalker core peak lies within was matched to a different FellWalker core. We also examined the brightest unmatched FellWalker cores whose peak positions did not lie within any SLC source boundaries, and in all cases we found that there were sources visible in the SCUBA Legacy map that were excluded from the final SCUBA Legacy catalogue. There were two causes for this exclusion. First, there were several bright emission peaks lying very close to a SCUBA Legacy map edge (these correspond to the brightest few open squares in each panel of Figure 18). Since many SCUBA Legacy maps suffer from significant edge artefacts, the SLC used strong criteria to eliminate potentially spurious objects identified near a map edge, and evidently on occasion those criteria also removed several real sources from their catalogue. Second, some peaks of emission were located within strong negative bowls in the SCUBA Legacy map: while the peaks themselves were bright enough to be easily discernable, their extents were truncated by the surrounding negative bowl to such an extent that these sources were likely eliminated by minimum size criteria imposed on the SLC. The apparent presence of bright unmatched FellWalker cores in Figure 16 and 17 are therefore not indicative of major inconsistencies between the SCUBA Legacy map and the SCUBA-2 map.

Finally, we show the effective completeness levels in the SCUBA catalogues by determining the fraction of SCUBA-2 cores found. Figure 19 shows the fraction of cores NWT07 identify in our SCUBA-2 catalogue as a function of peak flux (left panel) and total flux (right panel). The bin sizes adopted were chosen to ensure most bins were reasonably populated, while still showing sufficient detail at low fluxes. The vertical lines in both panels show the statistical / counting uncertainty based on the number of NWT07 cores in each bin, illustrating that most bins are not strongly

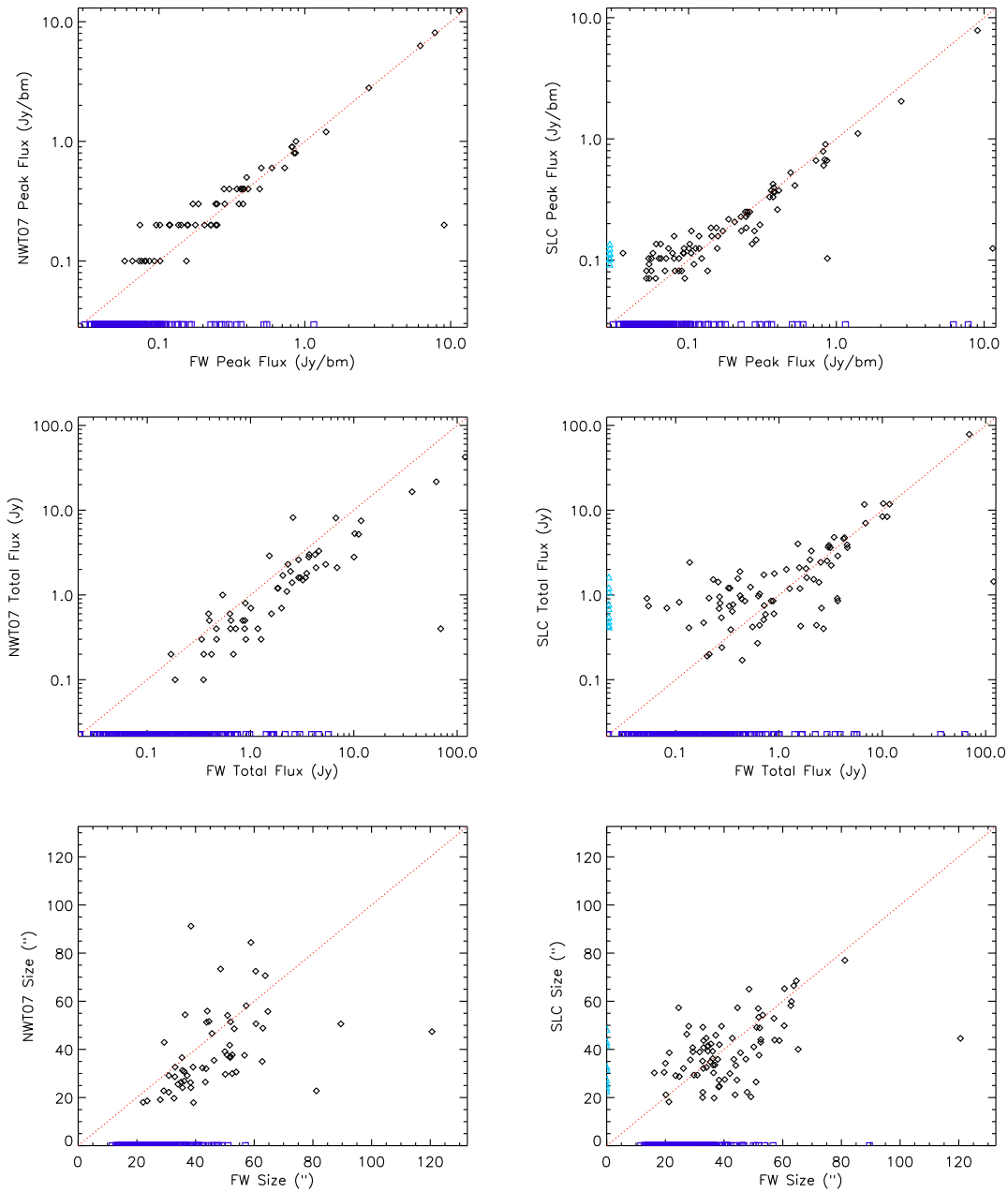

Figure 16. A comparison of cores identified in NGC 2023/2024 with SCUBA-2 data and SCUBA data by NWT07 (left) and the SLC (right). In each plot, the SCUBA-2 FellWalker core catalogue value is given on the horizontal axis, while the SCUBA catalogue value is given on the vertical axis. The top row shows the peak flux, while the middle row shows the total flux, and the bottom row shows the size (radius). A radius of 60″ corresponds to 0.12 pc at the distance of Orion B. Black diamonds show cores which had a match in both catalogues, while dark blue squares show cores only identified in the SCUBA-2 data and light blue triangles show cores only identified in the SCUBA data. The red dotted line indicates a one-to-one relationship.

populated. Still, it is clear that at higher peak and total flux values, the fraction of matches is generally good. We visually inspected the instances of fewer correspondences at higher peak and total fluxes and found that these were attributable to differences in how the FellWalker and ClumpFind algorithms divided complex emission structures into individual cores.

In the lower peak and total flux regimes, we find that the NWT07 catalogue is complete to roughly 40% to 60% of the cores in our catalogue at their nominal completeness level. For the peak flux, the completeness level shown (vertical dashed line) is five times the SCUBA noise level as listed in NWT07, which they state was used as the minimum ClumpFind threshold. The total flux completeness level is more difficult to determine, since it varies with core size. We roughly estimated the completeness level by taking a flux of three times the noise level across the average area of their cores[40]. Although there is a significant amount of uncertainty introduced by the complex emission structure,

[40] Normally, ClumpFind includes pixels within cores that have

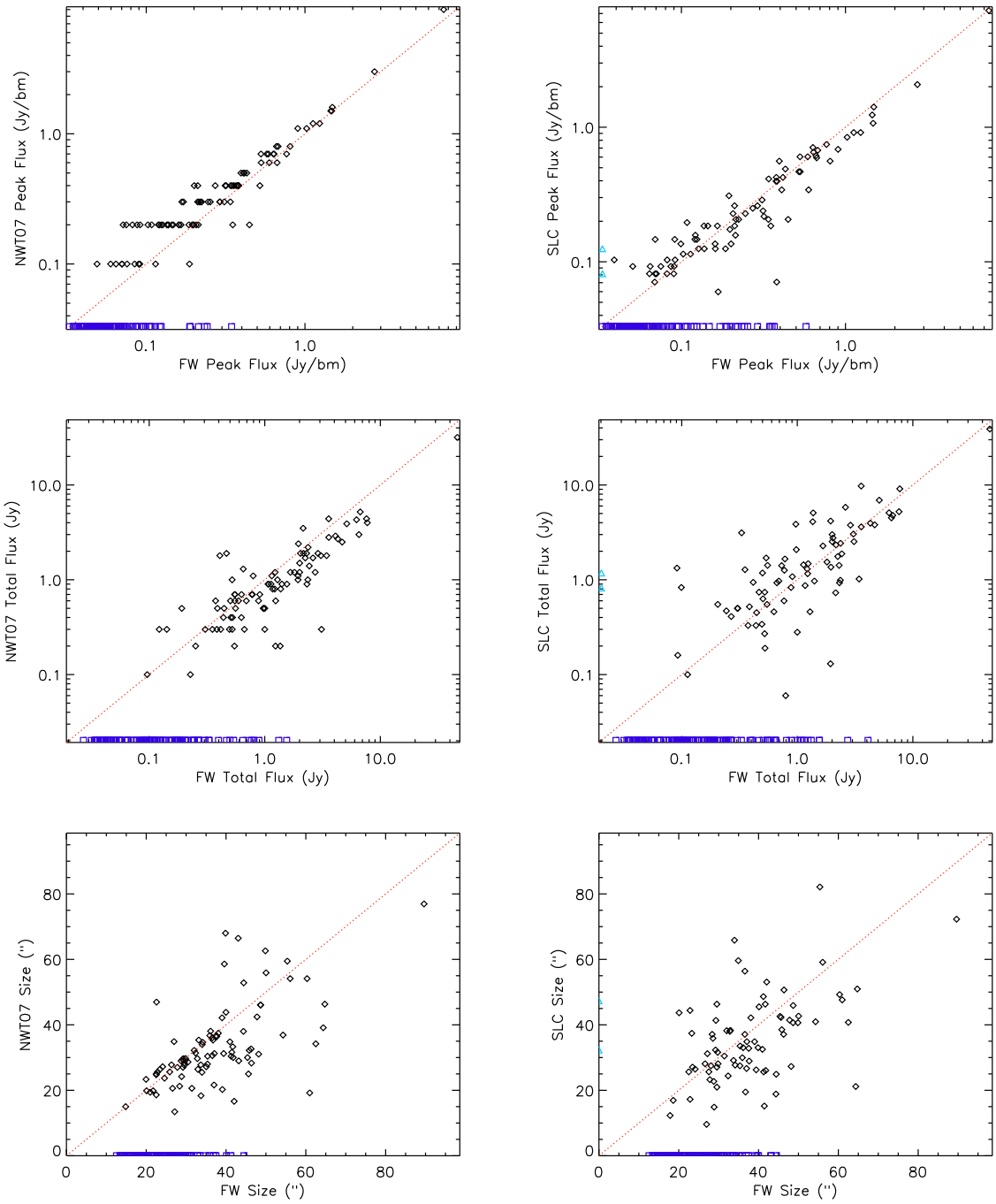

Figure 17. A comparison of cores identified in NGC 2068/2071 with SCUBA-2 data and SCUBA data by NWT07 (left) and the SLC (right). See Figure 16 for the plotting conventions used.

these comparisons suggest that the NWT07 catalogue would be roughly 90% complete at a completeness limit of approximately 50% higher than quoted in their paper.

These comparisons show that the SCUBA-2 data of Orion B analyzed here provide significantly more sensitive coverage than the SCUBA data (as well as also covering a larger area, as is evident comparing, e.g., Figures 3 and 14). With a typical noise level of ∼3.7 mJy bm^{-1}, our nominal 3 σ completeness is roughly 11 mJy bm^{-1} in peak flux, although we expect the actual value to be slightly larger, since faint cores lying outside of our external mask will have somewhat diminshed flux levels.

The authors thank the referee for a constructive report. The authors wish to recognize and acknowledge the very

fluxes down to 2 σ below the specified minimum peak flux value.

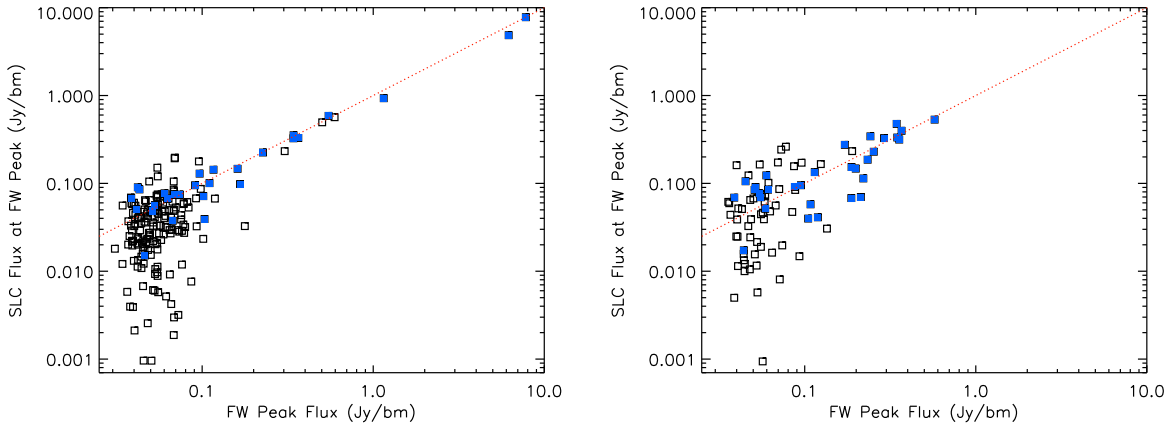

Figure 18. A comparison of flux values for FellWalker-identified cores not explicitly matched to an SLC entry. The horizontal axis shows the peak flux measured in the SCUBA-2 map for each un-matched FellWalker core. The vertical axis shows the flux in the SCUBA Legacy map at the location of the FellWalker core peak, while the red dotted line shows a one-to-one relationship. The filled blue squares show pixels in the SCUBA Legacy map which are associated with an SLC source (i.e., the FellWalker core is classified as 'unmatched' due to differences in core boundaries used by the two algorithms), while the black empty squares show pixels in the SCUBA Legacy map which are not associated with an SLC source. See text for details.

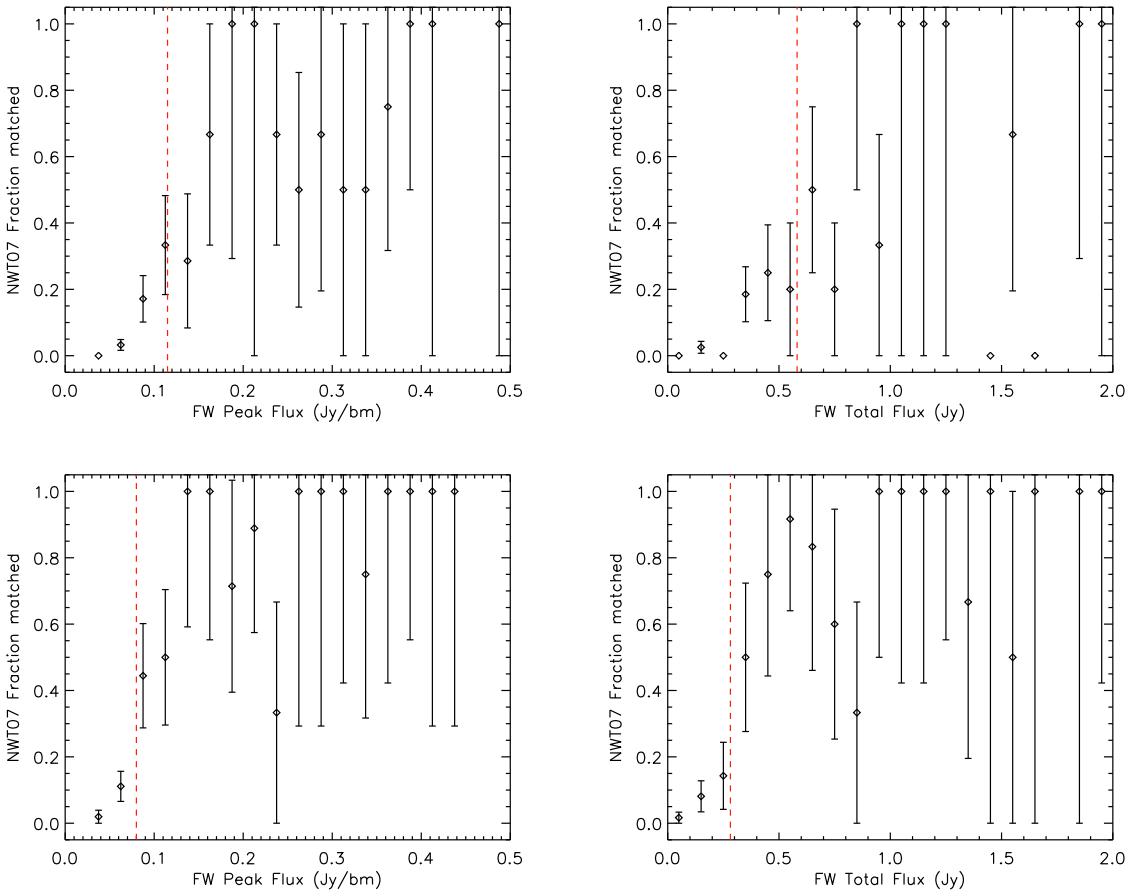

Figure 19. The fraction of our SCUBA-2 cores which have a match in the SCUBA catalogue of NWT07 for NGC 2023/2024 (top row) and NGC 2068/2071 (bottom row). The left panels show the fraction as a function of peak flux, binned to 0.025 Jy bm^{-1}, while the right panels show the fraction as a function of total flux, binned to 0.1 Jy. The vertical bars denote $\sqrt{(N)}$ counting statistics within the NWT07 catalogue, while the vertical (red) dashed lines give the approximate completeness levels in NWT07 (see text for details).

significant cultural role and reverence that the summit of Maunakea has always had within the indigenous Hawaiian community. We are most fortunate to have the opportunity to conduct observations from this mountain. The JCMT has historically been operated by the Joint Astronomy Centre on behalf of the Science and Technology Facilities

Council of the United Kingdom, the National Research Council of Canada and the Netherlands Organisation for Scientific Research. Additional funds for the construction of SCUBA-2 were provided by the Canada Foundation for Innovation. The identification number for the programme under which the SCUBA-2 data used in this paper is MJLSG41[41]. The authors thank the JCMT staff for their support of the GBS team in data collection and reduction efforts. The Starlink software (Currie et al. 2014) is supported by the East Asian Observatory. These data were reduced using a development version from December 2014 (version 516b455a). This research used the services of the Canadian Advanced Network for Astronomy Research (CANFAR) which in turn is supported by CANARIE, Compute Canada, University of Victoria, the National Research Council of Canada, and the Canadian Space Agency. This research used the facilities of the Canadian Astronomy Data Centre operated by the National Research Council of Canada with the support of the Canadian Space Agency. Figures in this paper were creating using the NASA IDL astronomy library (Landsman 1993) and the Coyote IDL library (`http://www.idlcoyote.com/index.html`).

REFERENCES

André, P., Di Francesco, J., Ward-Thompson, D., et al. 2014, Protostars and Planets VI, 27
André, P., Men'shchikov, A., Bontemps, S., et al. 2010, A&A, 518, L102
Anthony-Twarog, B. J. 1982, AJ, 87, 1213
Bally, J. 2008, Overview of the Orion Complex, ed. B. Reipurth, 459
Bally, J., Langer, W. D., Stark, A. A., & Wilson, R. W. 1987, ApJ, 312, L45
Berry, D. S. 2015, Astronomy and Computing, 10, 22
Berry, D. S., Reinhold, K., Jenness, T., & Economou, F. 2007, in Astronomical Society of the Pacific Conference Series, Vol. 376, Astronomical Data Analysis Software and Systems XVI, ed. R. A. Shaw, F. Hill, & D. J. Bell, 425
Bonnor, W. B. 1956, MNRAS, 116, 351
Buckle, J. V., Hills, R. E., Smith, H., et al. 2009, MNRAS, 399, 1026
Buckle, J. V., Curtis, E. I., Roberts, J. F., et al. 2010, MNRAS, 401, 204
Buckle, J. V., Drabek-Maunder, E., Greaves, J., et al. 2015, MNRAS, 449, 2472
Chapin, E., Gibb, A. G., Jenness, T., et al. 2013a, Starlink User Note, 258
Chapin, E. L., Berry, D. S., Gibb, A. G., et al. 2013b, MNRAS, 430, 2545
Currie, M. J., Berry, D. S., Jenness, T., et al. 2014, in Astronomical Society of the Pacific Conference Series, Vol. 485, Astronomical Data Analysis Software and Systems XXIII, ed. N. Manset & P. Forshay, 391
Dempsey, J. T., Friberg, P., Jenness, T., et al. 2013, MNRAS, 430, 2534
Di Francesco, J., Johnstone, D., Kirk, H., MacKenzie, T., & Ledwosinska, E. 2008, ApJS, 175, 277
Drabek, E., Hatchell, J., Friberg, P., et al. 2012, MNRAS, 426, 23
Ebert, R. 1955, ZAp, 37, 217
Enoch, M. L., Evans, II, N. J., Sargent, A. I., et al. 2008, ApJ, 684, 1240
Enoch, M. L., Glenn, J., Evans, II, N. J., et al. 2007, ApJ, 666, 982
Enoch, M. L., Young, K. E., Glenn, J., et al. 2006, ApJ, 638, 293
Hartmann, L. 1998, Accretion Processes in Star Formation
Hatchell, J., Fuller, G. A., Richer, J. S., Harries, T. J., & Ladd, E. F. 2007, A&A, 468, 1009
Hatchell, J., Richer, J. S., Fuller, G. A., et al. 2005, A&A, 440, 151
Hatchell, J., Wilson, T., Drabek, E., et al. 2013, MNRAS, 429, L10
Hildebrand, R. H. 1983, QJRAS, 24, 267
Holland, W. S., Bintley, D., Chapin, E. L., et al. 2013, MNRAS, 430, 2513
Jenness, T., Currie, M. J., Tilanus, R. P. J., et al. 2015, MNRAS, 453, 73
Jessop, N. E., & Ward-Thompson, D. 2000, MNRAS, 311, 63
Johnstone, D., Boonman, A. M. S., & van Dishoeck, E. F. 2003, A&A, 412, 157
Johnstone, D., Di Francesco, J., & Kirk, H. 2004, ApJ, 611, L45
Johnstone, D., Fich, M., Mitchell, G. F., & Moriarty-Schieven, G. 2001, ApJ, 559, 307
Johnstone, D., Matthews, H., & Mitchell, G. F. 2006, ApJ, 639, 259
Jørgensen, J. K., Johnstone, D., Kirk, H., & Myers, P. C. 2007, ApJ, 656, 293
Jørgensen, J. K., Johnstone, D., Kirk, H., et al. 2008, ApJ, 683, 822
Kackley, R., Scott, D., Chapin, E., & Friberg, P. 2010, in Society of Photo-Optical Instrumentation Engineers (SPIE) Conference Series, Vol. 7740, Society of Photo-Optical Instrumentation Engineers (SPIE) Conference Series, 1
Kirk, H., Johnstone, D., & Di Francesco, J. 2006, ApJ, 646, 1009
Kirk, H., Johnstone, D., & Tafalla, M. 2007, ApJ, 668, 1042
Kirk, J. M., Ward-Thompson, D., & André, P. 2005, MNRAS, 360, 1506
Könyves, V., André, P., Schneider, N., et al. 2013, Astronomische Nachrichten, 334, 908
Lada, C. J., Muench, A. A., Rathborne, J., Alves, J. F., & Lombardi, M. 2008, ApJ, 672, 410
Lada, E. A., Bally, J., & Stark, A. A. 1991, ApJ, 368, 432
Landsman, W. B. 1993, in Astronomical Society of the Pacific Conference Series, Vol. 52, Astronomical Data Analysis Software and Systems II, ed. R. J. Hanisch, R. J. V. Brissenden, & J. Barnes, 246
Lombardi, M., Alves, J., & Lada, C. J. 2011, A&A, 535, A16
Lombardi, M., Bouy, H., Alves, J., & Lada, C. J. 2014, A&A, 566, A45
Maddalena, R. J., Morris, M., Moscowitz, J., & Thaddeus, P. 1986, ApJ, 303, 375
Mairs, S., Johnstone, D., Offner, S. S. R., & Schnee, S. 2014, ApJ, 783, 60
Mairs, S., Johnstone, D., Kirk, H., et al. 2015, MNRAS, 454, 2557
Matthews, B. C., Fiege, J. D., & Moriarty-Schieven, G. 2002, ApJ, 569, 304
Matthews, B. C., & Wilson, C. D. 2002, ApJ, 571, 356
McKee, C. F. 1989, ApJ, 345, 782
Megeath, S. T., Gutermuth, R., Muzerolle, J., et al. 2012, AJ, 144, 192

[41] One scan in NGC 2023/2024 (target OrionB_450_S) is presently mis-labelled in CADC with the project code MJLSG31 (the designation for Orion A). Observations taken during science verification across all GBS regions falls under the project code MJLSG22

Menten, K. M., Reid, M. J., Forbrich, J., & Brunthaler, A. 2007, A&A, 474, 515
Meyer, M. R., Flaherty, K., Levine, J. L., et al. 2008, Star Formation in NGC 2023, NGC 2024, and Southern L1630, ed. B. Reipurth, 662
Mitchell, G. F., Johnstone, D., Moriarty-Schieven, G., Fich, M., & Tothill, N. F. H. 2001, ApJ, 556, 215
Motte, F., André, P., Ward-Thompson, D., & Bontemps, S. 2001, A&A, 372, L41
Muench, A., Getman, K., Hillenbrand, L., & Preibisch, T. 2008, Star Formation in the Orion Nebula I: Stellar Content, ed. B. Reipurth, 483
Nutter, D., & Ward-Thompson, D. 2007, MNRAS, 374, 1413
Onishi, T., Mizuno, A., Kawamura, A., Ogawa, H., & Fukui, Y. 1998, ApJ, 502, 296
Pattle, K., Ward-Thompson, D., Kirk, J. M., et al. 2015, MNRAS, 450, 1094
Reipurth, B., Megeath, S. T., Bally, J., & Walawender, J. 2008, The L1617 and L1622 Cometary Clouds in Orion, ed. B. Reipurth, 782
Rosolowsky, E. W., Pineda, J. E., Kauffmann, J., & Goodman, A. A. 2008, ApJ, 679, 1338
Sadavoy, S. I., Di Francesco, J., Bontemps, S., et al. 2010, ApJ, 710, 1247
Sadavoy, S. I., Di Francesco, J., Johnstone, D., et al. 2013, ApJ, 767, 126
Salji, C. J., Richer, J. S., Buckle, J. V., et al. 2015, MNRAS, 449, 1769
Salpeter, E. E. 1955, ApJ, 121, 161
Schneider, N., André, P., Könyves, V., et al. 2013, ApJ, 766, L17
Stutz, A. M., Tobin, J. J., Stanke, T., et al. 2013, ApJ, 767, 36
van Kempen, T. A., van Dishoeck, E. F., Salter, D. M., et al. 2009, A&A, 498, 167
Ward-Thompson, D., Di Francesco, J., Hatchell, J., et al. 2007, PASP, 119, 855
Watson, M. 2010, Master's thesis, University of Hertfordshire
Williams, J. P., de Geus, E. J., & Blitz, L. 1994, ApJ, 428, 693

Table 4
Dense Cores Identified with Fellwalker

Source Name MJLSG	Region	Index	R.A.[a] (J2000.0)	Dec.[a] (J2000.0)	850 μm Peak [b] (Jy bm^{-1})	850 μm Total [b] (Jy)	R_{eff} [b] (pc)	450 μm Peak [c] (Jy bm^{-1})	450 μm Total [c] (Jy)	YSO[d]	Cov.[e]	CO C Pe (Jy b
J055424.5+014419	L1622	1	5:54:24.60	+01:44:19.7	1.200	4.889	0.121	4.656	27.708	Y	0.00	-
J055412.3+014234	L1622	2	5:54:12.39	+01:42:34.7	0.202	2.013	0.108	0.985	10.506	Y	0.00	-
J055440.2+015404	L1622	3	5:54:40.21	+01:54:04.7	0.138	1.714	0.135	0.772	6.288	N	0.00	-
J055403.3+014025	L1622	4	5:54:03.39	+01:40:25.7	0.115	0.174	0.043	0.647	0.775	N	0.00	-
J055406.1+014255	L1622	5	5:54:06.19	+01:42:55.7	0.110	0.665	0.073	0.730	3.043	N	0.00	-
J055429.7+014737	L1622	6	5:54:29.80	+01:47:37.7	0.101	0.782	0.081	0.746	3.132	Y	0.00	-
J055453.4+015837	L1622	7	5:54:53.41	+01:58:37.7	0.088	0.273	0.057	0.608	0.978	N	0.00	-
J055440.0+014340	L1622	8	5:54:40.00	+01:43:40.7	0.088	0.241	0.060	0.604	0.369	N	0.00	-
J055421.7+014210	L1622	9	5:54:21.79	+01:42:10.7	0.080	0.370	0.063	0.875	1.608	N	0.00	-
J055419.9+015040	L1622	10	5:54:19.99	+01:50:40.7	0.080	0.234	0.054	0.712	1.233	Y	0.00	-
J055428.1+014716	L1622	11	5:54:28.20	+01:47:16.7	0.074	0.143	0.042	0.514	0.524	N	0.00	-
J055426.3+014152	L1622	12	5:54:26.40	+01:41:52.7	0.063	0.155	0.051	0.610	0.497	N	0.00	-
J055418.1+014913	L1622	13	5:54:18.19	+01:49:13.7	0.062	0.248	0.061	0.726	1.283	Y	0.00	-
J055426.9+015213	L1622	14	5:54:27.00	+01:52:13.7	0.057	0.093	0.042	0.610	0.396	N	0.00	-
J055459.6+020401	L1622	15	5:54:59.62	+02:04:01.7	0.057	0.082	0.044	0.744	-0.016	N	0.00	-
J055445.6+014940	L1622	16	5:54:45.61	+01:49:40.7	0.056	0.103	0.047	0.740	0.456	N	0.00	-
J055355.5+014110	L1622	17	5:53:55.58	+01:41:10.7	0.053	0.185	0.064	0.683	1.411	N	0.00	-
J055431.1+014858	L1622	18	5:54:31.20	+01:48:58.7	0.049	0.084	0.042	0.554	0.325	N	0.00	-
J055415.5+014046	L1622	19	5:54:15.59	+01:40:46.7	0.049	0.100	0.048	0.625	0.428	N	0.00	-
J055507.8+014513	L1622	20	5:55:07.82	+01:45:13.7	0.045	0.027	0.026	0.491	0.046	N	0.00	-
J055429.7+015340	L1622	21	5:54:29.80	+01:53:40.7	0.045	0.114	0.055	0.625	0.395	N	0.00	-
J055441.6+014046	L1622	22	5:54:41.60	+01:40:46.7	0.045	0.103	0.048	0.573	0.440	N	0.00	-
J055509.6+015637	L1622	23	5:55:09.62	+01:56:37.7	0.044	0.027	0.025	0.458	-0.045	N	0.00	-
J055505.2+020040	L1622	24	5:55:05.22	+02:00:40.7	0.044	0.104	0.048	0.677	0.496	N	0.00	-
J055443.6+015040	L1622	25	5:54:43.60	+01:50:40.7	0.042	0.042	0.031	0.567	0.109	N	0.00	-
J055408.5+015046	L1622	26	5:54:08.59	+01:50:46.7	0.042	0.033	0.028	0.545	0.122	N	0.00	-
J055452.0+015734	L1622	27	5:54:52.01	+01:57:34.7	0.041	0.077	0.046	0.630	0.171	N	0.00	-
J055435.0+015210	L1622	28	5:54:35.00	+01:52:10.7	0.041	0.085	0.046	0.654	0.461	N	0.00	-
J055451.8+014513	L1622	29	5:54:51.81	+01:45:13.7	0.038	0.055	0.037	0.515	0.237	N	0.00	-
J054705.0+002145	N2068/2071	1	5:47:05.00	+00:21:45.1	7.459	46.389	0.180	28.247	320.114	Y	1.00	7.
J054608.6-001044	N2068/2071	2	5:46:08.61	-00:10:44.6	2.736	5.122	0.084	7.017	25.257	Y	0.00	-
J054607.4-001335	N2068/2071	3	5:46:07.41	-00:13:35.5	1.484	7.711	0.113	7.586	53.072	Y	0.00	-
J054724.9+002100	N2068/2071	4	5:47:25.00	+00:21:00.1	1.469	7.594	0.130	6.047	50.139	Y	1.00	1.
J054631.2-000235	N2068/2071	5	5:46:31.21	-00:02:35.7	1.452	4.287	0.109	5.995	22.861	N	0.00	-
J054628.0-000053	N2068/2071	6	5:46:28.01	-00:00:53.7	1.234	4.674	0.093	3.937	26.024	Y	0.00	-
J054647.6+000027	N2068/2071	7	5:46:47.60	+00:00:27.2	1.121	6.530	0.126	4.019	48.016	Y	0.00	-
J054628.4+001927	N2068/2071	8	5:46:28.40	+00:19:27.1	1.021	2.611	0.074	3.203	12.709	Y	1.00	1.
J054710.7+002112	N2068/2071	9	5:47:10.80	+00:21:12.1	0.899	2.301	0.079	3.767	17.659	Y	1.00	0.
J054701.1+002621	N2068/2071	10	5:47:01.20	+00:26:21.1	0.804	3.428	0.130	2.657	16.280	Y	0.84	0.
J054608.4-000959	N2068/2071	11	5:46:08.41	-00:09:59.6	0.764	2.885	0.073	3.087	20.289	Y	0.00	-
J054650.0+000203	N2068/2071	12	5:46:50.00	+00:02:03.2	0.675	6.225	0.121	2.715	48.999	N	0.00	-
J054610.2-001217	N2068/2071	13	5:46:10.21	-00:12:17.6	0.666	1.373	0.068	2.129	7.426	Y	0.00	-
J054639.6+000112	N2068/2071	14	5:46:39.60	+00:01:12.2	0.659	2.165	0.071	2.885	14.478	Y	0.00	-
J054638.0+000036	N2068/2071	15	5:46:38.00	+00:00:36.2	0.637	2.429	0.056	2.325	16.487	Y	0.00	-
J054607.8-001153	N2068/2071	16	5:46:07.81	-00:11:53.6	0.631	1.943	0.060	2.308	13.678	N	0.00	-
J054603.8-001450	N2068/2071	17	5:46:03.81	-00:14:50.5	0.594	1.407	0.074	2.650	7.729	Y	0.00	-
J054648.2+000133	N2068/2071	18	5:46:48.21	+00:01:33.2	0.587	6.701	0.101	2.457	52.950	Y	0.00	-
J054706.5+002239	N2068/2071	19	5:47:06.60	+00:22:39.1	0.573	4.093	0.072	1.443	20.561	Y	1.00	0.
J054807.8+003351	N2068/2071	20	5:48:07.80	+00:33:51.1	0.572	1.198	0.089	1.790	5.914	Y	0.00	-
J054737.1+002006	N2068/2071	21	5:47:37.20	+00:20:06.1	0.528	2.037	0.077	2.695	16.638	Y	1.00	0.
J054643.0+000048	N2068/2071	22	5:46:43.00	+00:00:48.2	0.527	3.580	0.074	2.099	27.452	Y	0.00	-
J054608.0-001220	N2068/2071	23	5:46:08.01	-00:12:20.6	0.518	0.971	0.040	1.719	5.744	Y	0.00	-
J054606.2-000935	N2068/2071	24	5:46:06.21	-00:09:35.6	0.446	3.096	0.123	1.452	18.379	Y	0.00	-
J054640.6+000033	N2068/2071	25	5:46:40.61	+00:00:33.2	0.429	2.240	0.058	1.754	16.919	N	0.00	-
J054627.0+000109	N2068/2071	26	5:46:27.01	+00:01:09.2	0.415	1.668	0.064	1.391	10.701	N	0.00	-
J054732.7+002024	N2068/2071	27	5:47:32.80	+00:20:24.1	0.407	1.132	0.059	1.707	9.052	Y	1.00	0.
J054645.8+000721	N2068/2071	28	5:46:45.80	+00:07:21.2	0.394	3.573	0.111	1.628	27.688	N	0.00	-
J054624.4-000002	N2068/2071	29	5:46:24.41	-00:00:02.7	0.381	3.059	0.096	1.286	20.452	N	0.00	-
J054635.4+000030	N2068/2071	30	5:46:35.41	+00:00:30.2	0.380	1.939	0.083	1.458	13.511	N	0.00	-
J054628.2-000135	N2068/2071	31	5:46:28.21	-00:01:35.7	0.378	2.004	0.066	1.275	10.651	N	0.00	-
J054706.8+001230	N2068/2071	32	5:47:06.80	+00:12:30.2	0.377	1.807	0.082	1.302	12.402	N	1.00	0.
J054743.6+003821	N2068/2071	33	5:47:43.60	+00:38:21.1	0.370	1.080	0.070	1.224	5.612	Y	0.00	-
J054629.6+002012	N2068/2071	34	5:46:29.60	+00:20:12.1	0.367	2.730	0.087	1.230	13.842	N	1.00	0.
J054605.0-001417	N2068/2071	35	5:46:05.01	-00:14:17.5	0.356	1.079	0.052	1.567	6.254	Y	0.00	-
J054745.2+003842	N2068/2071	36	5:47:45.20	+00:38:42.1	0.354	1.054	0.074	1.111	5.761	N	0.00	-
J054613.2-000605	N2068/2071	37	5:46:13.21	-00:06:05.7	0.350	0.666	0.063	1.581	5.214	Y	0.00	-
J054645.2+000018	N2068/2071	38	5:46:45.20	+00:00:18.3	0.347	1.149	0.045	1.337	9.250	N	0.00	-
J054647.2+000724	N2068/2071	39	5:46:47.20	+00:07:24.2	0.344	1.547	0.075	1.272	11.869	N	0.00	-
J054701.8+001806	N2068/2071	40	5:47:01.80	+00:18:06.1	0.339	2.369	0.098	1.152	14.131	Y	1.00	0.
J054702.3+002048	N2068/2071	41	5:47:02.40	+00:20:48.1	0.338	2.358	0.069	0.871	8.079	N	1.00	0.
J054712.8+002221	N2068/2071	42	5:47:12.80	+00:22:21.1	0.318	1.169	0.060	1.363	8.162	N	1.00	0.
J054716.1+002124	N2068/2071	43	5:47:16.20	+00:21:24.1	0.313	1.288	0.074	1.242	8.314	N	1.00	0.
J054633.6-000008	N2068/2071	44	5:46:33.61	-00:00:08.7	0.310	0.906	0.049	1.329	6.665	Y	0.00	-
J054627.6+000133	N2068/2071	45	5:46:27.61	+00:01:33.2	0.290	1.068	0.071	1.087	7.002	N	0.00	-
J054632.4-000041	N2068/2071	46	5:46:32.41	-00:00:41.7	0.290	0.692	0.045	0.998	4.565	N	0.00	-
J054657.2+002009	N2068/2071	47	5:46:57.20	+00:20:09.1	0.271	2.319	0.097	0.528	4.479	N	1.00	0.
J054735.3+002021	N2068/2071	48	5:47:35.40	+00:20:21.1	0.253	0.552	0.040	1.176	4.598	N	1.00	0.
J054725.1+003506	N2068/2071	49	5:47:25.20	+00:35:06.1	0.247	1.606	0.102	0.662	7.059	N	0.00	-